



Parametric modeling and multiobjective crashworthiness design optimization of a new front longitudinal beam

Libin Duan¹ · Haobin Jiang¹ · Guoqing Geng¹ · Xuerong Zhang¹ · Zhanjiang Li²

Received: 12 July 2018 / Revised: 17 October 2018 / Accepted: 23 October 2018 / Published online: 20 November 2018
© Springer-Verlag GmbH Germany, part of Springer Nature 2018

Abstract

The front longitudinal beam (FLB) is the most important energy-absorbing and crashing force-transmitting structure of a vehicle under front-impact collision. For better weight reduction and crashworthiness of the FLB, a new structure, variable rolled blank-variable cross-sectional shape FLB (VRB-VCS FLB), is proposed. It has both the continuous variation of thickness and variable cross-sectional shape in space. As the thickness distribution and cross-sectional shape change continuously, the proposed structure evolves into three distinct forms, i.e., the uniform-thickness FLB, variable rolled blank FLB, and variable cross-sectional shape FLB. However, literature on parametric modeling and crashworthiness design optimization of the VRB-VCS FLB is very limited. This paper proposes a parametric modeling method of VRB-VCS FLB with manufacturing constraints. Multiobjective crashworthiness design optimization is performed to explore the lightweightness and crashworthiness performance of the VRB-VCS FLB. Firstly, thickness distribution and cross-sectional shape parameters are defined. Secondly, local parametric subsystem front-impact model is established to balance accuracy and efficiency. Thirdly, a multiobjective optimization model of VRB-VCS FLB is constructed. Finally, a fully automated design of experiment platform is established to improve the data collection efficiency, and epsilon-support vector regression technique and non-dominated sorting genetic algorithm II are utilized to search the Pareto optimal frontier. The numerical results show that the lightweightness and crashworthiness of the VRB-VCS FLB are significantly improved when compared with the uniform-thickness FLB.

Keywords Parametric modeling · Multiobjective crashworthiness optimization · Front longitudinal beam (FLB) · Variable rolled blank (VRB) · Variable cross-sectional shape (VCS)

Nomenclature

CTZ	Constant-thickness zone	SEA	Specific energy absorption
FLB	Front longitudinal beam	TTZ	Thickness transition zone
FLB-inner	FLB inner plate	UT FLB	Uniform-thickness FLB
FLB-outer	FLB outer plate	UT FLB-inner	Uniform-thickness FLB inner plate
MOO	Multiobjective optimization	VCS	Variable cross-sectional shape
NSGA-II	Non-dominated sorting genetic algorithm II	VCS FLB	Variable cross-sectional shape FLB
OLHS	Optimal Latin hypercube sampling	VRB	Variable rolled blank
PCF	Peak crushing force	VRB FLB	Variable rolled blank FLB
		VRB-VCS FLB	Variable rolled blank-variable cross-sectional shape FLB
		VRB-VCS FLB-inner	VRB-VCS FLB inner plate
		ϵ -SVR	Epsilon-support vector regression

Responsible Editor: Emilio Carlos Nelli Silva

✉ Haobin Jiang
jianghb@ujs.edu.cn

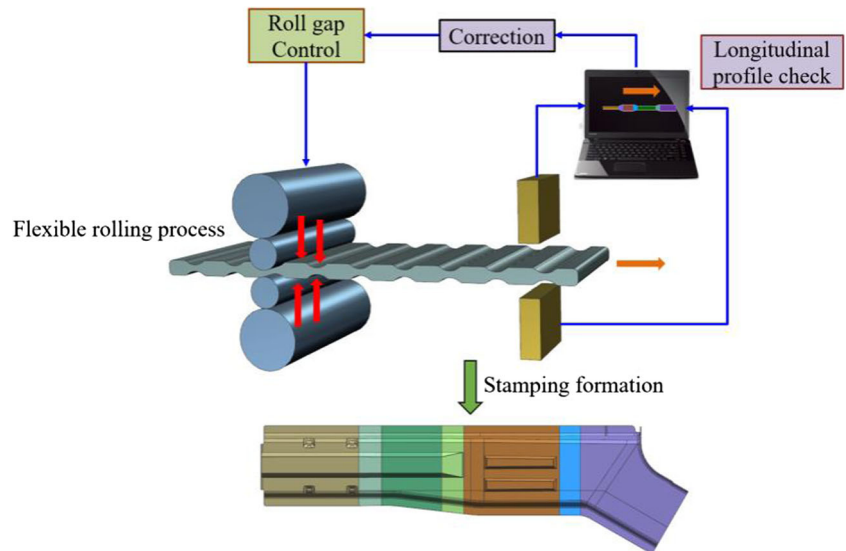
¹ School of Automotive and Traffic Engineering, Jiangsu University, Zhenjiang 212013, China

² Nanjing Yuebo Power System Co., Ltd., Nanjing, China

1 Introduction

Owing to the increasing demands for high-energy absorption and lightweighting, thin-walled structures are widely used in automotive industry. Among the thin-walled structures, front

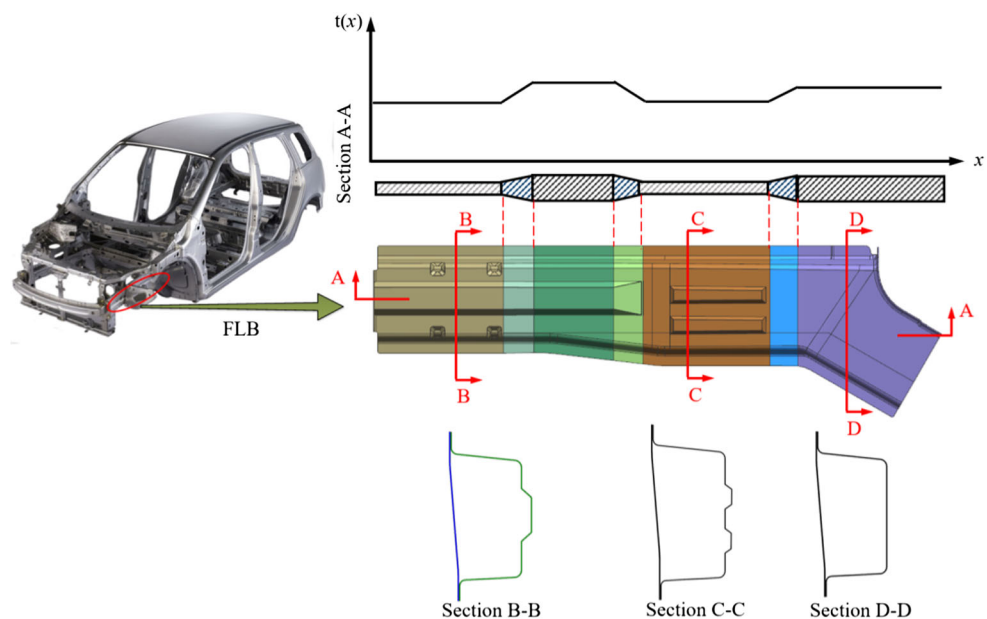
Fig. 1 Flexible rolling process of variable rolled blanks



longitudinal beam (FLB) is the significant deformable part and energy absorption structure under vehicle front-impact collision. The design quality of FLB will directly determine the vehicle safety to some extent. The conventional FLB is mainly made of thin-walled structure with uniform thickness (UT). Its structure is simple, and relevant research has matured. The inherent shortcoming is that such structure may not exert their maximum capacities in crashworthiness and lightweightness. To address this issue, cross-sectional shape optimization for uniform-thickness FLB (UT FLB) provides an effective way to improve energy absorption capabilities. Over the past few decades, the crashworthiness of thin-walled structures with various geometric sections has been investigated, such as polygonal (Alavi Nia and Parsapour 2014; Ali et al. 2015; Nia and Hamedani 2010;

Pirmohammad and Saravani 2018) and multicell (Hou et al. 2008; Tang et al. 2012; Zhang and Zhang 2013; Tran et al. 2015; Tran 2017; Usta et al. 2018) sections. Later, researchers have designed the variable cross-sectional shape FLB (VCS FLB) (Chahardoli and Nia 2017; Hao et al. 2017; Qiu et al. 2018) and carried out necessary studies on it. Elmarakbi et al. (2013) and Beik et al. (2016) studied the influence of different cross-sectional geometries on the crashing energy absorption of S-shaped FLBs. Liu et al. (2014) adopted maximized specific energy absorption (SEA) as the objective function and suggested improvements for the crashing energy absorption of S-shaped FLBs by optimizing the cross-sectional geometry. Duddeck et al. (2016) took mass minimization as the objective function and used hybrid cellular automata to optimize the cross-sectional configuration of the VCS thin-walled

Fig. 2 Illustration of the proposed VRB-VCS FLB structure



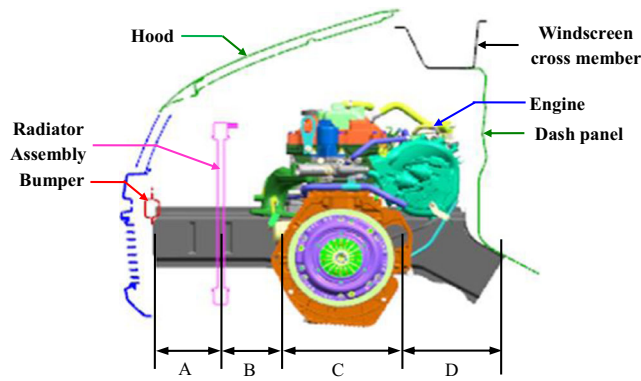


Fig. 3 Crash space management for FLB (Duan et al. 2016)

structure. Wu et al. (2017) performed multiobjective design optimization on the crashworthiness of varying Fourier section tubes to maximize the SEA and minimize the peak crushing force (PCF). Wang and Qiu (2018) performed the lightweightness and crashworthiness design optimization of a VCS-tapered beam to minimize the mass and PCF. Cai and Wang (2017a) constructed implicit parametric models of VCS FLBs and performed multiobjective crashworthiness optimization on the structure to maximize the SEA and minimize PCF. Hunkeler et al. (2013) established implicit parametric models of the structure and optimized its cross-sectional geometry. Aiming to minimize the mass and maximize energy absorption, Montoya et al. (2015) and Rais-Rohani et al. (2006) carried out multiobjective optimization on VCS FLB structures. However, these crashworthiness optimizations of the past yield only the best cross-sectional shapes for VCS FLBs under specific thickness and they are unable to alter the thickness distribution among the different functional regions of the structure in response to the collision load or to maximize the material utilization.

As the technique for variable rolled blanks (VRBs) matures, computerized real-time control and adjustment of roller distance during flexible rolling produces VRB plates with continuously changing thickness as preset along the direction of rolling, as shown in Fig. 1. Liu (2011) studied the flexible rolling process of VRBs in-depth and proposed differential equations for force balance during variable-

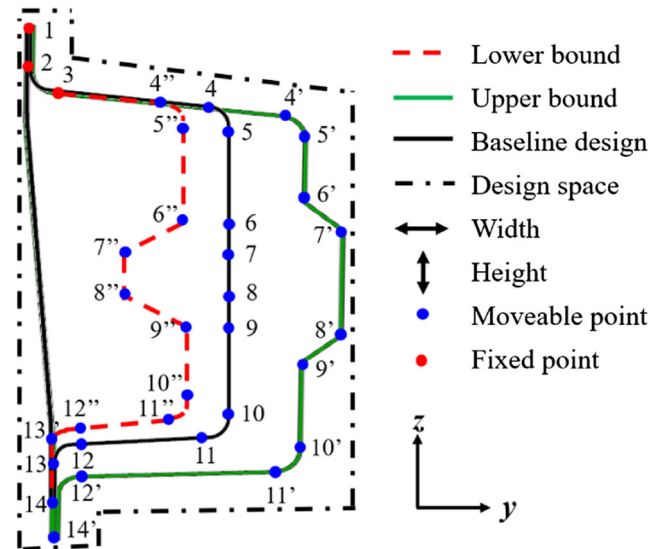
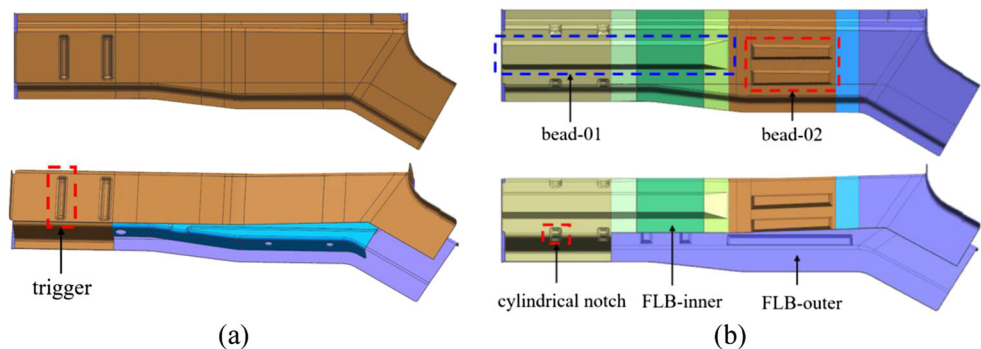


Fig. 5 Implicit parameterization for the cross-sectional shape of VCS FLB

thickness rolling and mass conservation equations, which lay the theoretical foundation for studying the mechanics and kinematics of VRB flexible rolling. On this basis, the manufacturing of VRB FLB structure could be realized (Kopp et al. 2005; Meyer et al. 2008; Kim et al. 2014). Some researchers (e.g., Lu et al. (2017), Rajabiehfarid et al. (2016), Zhang and Zhang (2016), and Mohammadiha and Ghariblu (2017)) investigated the energy absorption of VRB thin-walled structures during crashing deformation by means of experiments and numerical simulations. The results show far superior crashing energy absorption of the structure than its uniform-thickness counterpart. Despite its excellent crashworthiness and lightweighting potential, the optimal thickness distribution in the VRB FLB structure is difficult to obtain. For the time being, engineers mostly optimize the structure by observing its deformation and internal energy distribution and through trial and error. However, the traditional trial-and-error method has many shortcomings, such as the inability to obtain the optimal thickness distribution for the structure, low design efficiency, and long design cycle. As an alternative to overcome these problems, numerical optimization is a good

Fig. 4 Comparison of the conventional UT FLB and the proposed VRB-VCS FLB. a UT FLB. b VRB-VCS FLB



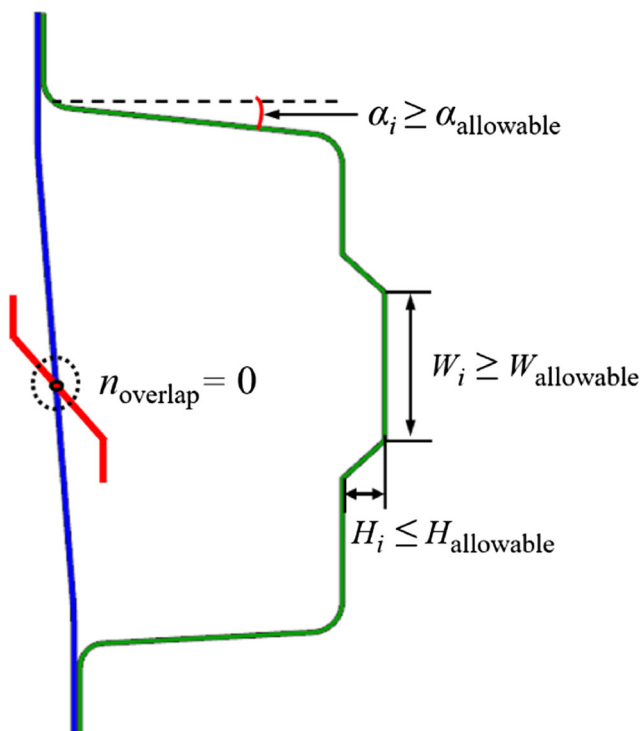


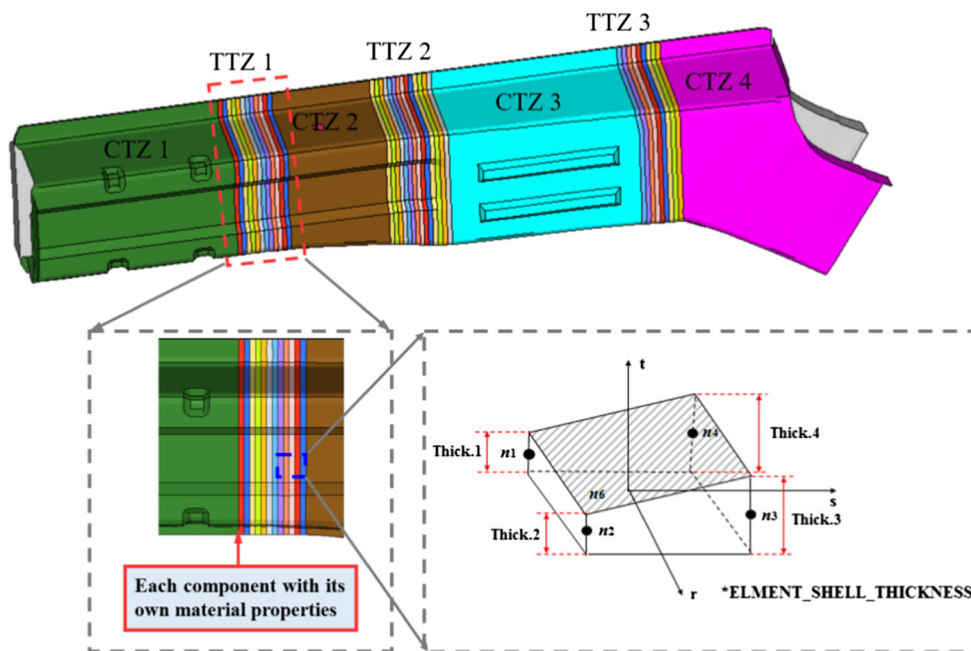
Fig. 6 Illustration of stamping constraints for the cross section of a VCS FLB

solution for the efficient design of automobile VRB FLBs. Sun et al. (2014) proposed a functionally graded thickness (FGT) tube and identified the thickness gradient for achieving the best crashworthiness characteristics through multiobjective optimization study. In this regards, Li et al. (2015), Fang et al. (2015), Zhang et al. (2015), Xu et al.

(2018), and Ying et al. (2017) investigated the influence of the thickness gradient on the crashworthiness of the FGT tube and carried out multiobjective crashworthiness optimization on this structure. In fact, the automobile VRB FLBs typically consist of constant-thickness zone (CTZ) and thickness transition zone (TTZ). However, the aforementioned studies did not consider the effects of the thickness of CTZ and the length and number of TTZ on the crashworthiness of VRB FLBs. For this reason, Duan et al. (2017a; Duan et al. 2016) constructed a parametric model on the thickness distribution of VRB FLB structure with the thickness of the CTZ and length and position of the TTZ as design parameters, and they performed lightweighting and crashworthiness optimization. However, as the crashworthiness optimization of VRB FLBs gives only the optimal thickness distribution for certain cross sections, it is difficult to improve vehicle lightweighting and crashworthiness further by only optimizing the thickness distribution of the beam material.

The above results show the apparent weakness of the existing structural optimization on VCS FLBs or VRB FLBs for vehicle lightweighting and crashworthiness improvement. In this research, a new type of VRB-VCS FLB structure is proposed. It possesses both the continuous variation of thickness and variable cross-sectional shape in design space, as shown in Fig. 2. As the thickness distribution and cross-sectional shape change continuously, the proposed structure evolves into three distinct forms: the UT FLB, VCS FLB, and VRB FLB. Thus, the VRB-VCS FLB results from the improvement and development in these three structures and combines their advantages to achieve greater generality and more-promising engineering application prospects. To this

Fig. 7 FE model of the VRB-VCS FLB structure



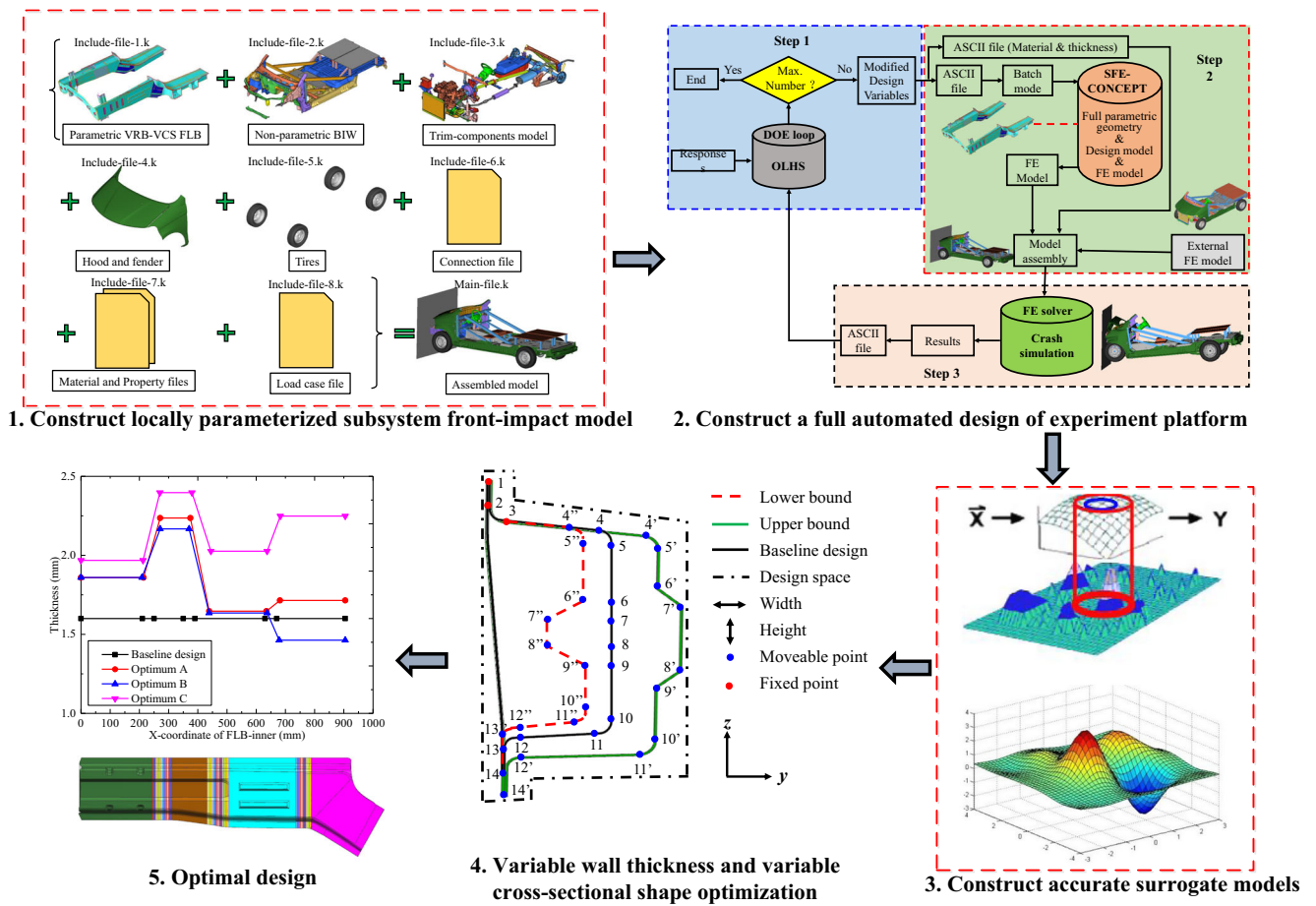


Fig. 8 Optimization process for VRB-VCS FLB. (1) Construct a locally parameterized subsystem front-impact model. (2) Construct a fully automated design of experiment platform. (3) Construct accurate surrogate models. (4) Variable wall thickness and variable cross-sectional shape optimization. (5) Optimal design

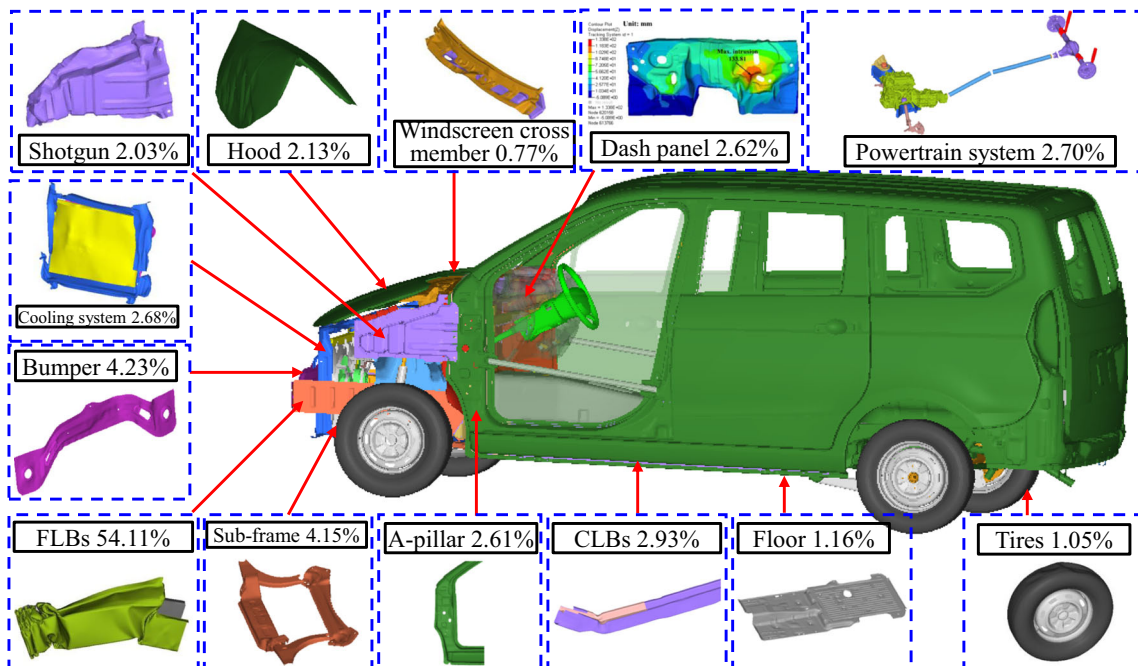
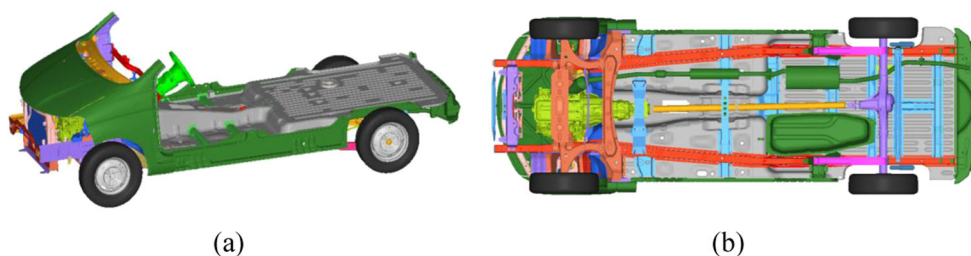


Fig. 9 Illustration of the key energy-absorbing components

Fig. 10 Illustration of the initial subsystem model. **a** ISO view. **b** Bottom view



end, VRB-VCS FLB offers greater design space and freedom in the early design phase of vehicles and enhances the lightweightness and collision resistance of the car.

To make use of VRB-VCS FLB in automotive industry, it is essential to investigate its crashworthiness and lightweighting potential. To the author's best knowledge, however, investigation on the VRB-VCS FLB structure is very limited, and achieving crashworthiness and lightweightness in VRB-VCS FLB at the same time could be difficult. Therefore, multiobjective design optimization on the structure is required. Moreover, studies on parametric modeling of VRB-VCS FLB are very limited. The purpose of this paper is not only to establish a full parametric model of VRB-VCS FLB but also to provide an efficient multiobjective crashworthiness optimization design strategy for the VRB-VCS FLB. For this reason, the work is organized as follows: Section 2 presents the basic principles of crashworthiness design of FLB under front-impact collision; Section 3 proposes the parametric modeling method of the VRB-VCS FLB structure. Section 4 gives the detailed multiobjective crashworthiness optimization process of VRB-VCS FLB, followed by the results and discussions. Conclusions and further works are given in Section 5 to close the paper.

2 Crashworthiness design of FLB under front-impact collision

The FLB crash space management method proposed in the literature (Duan et al. 2016) states that the FLB of a front engine passenger car can be divided into four functional regions (Fig. 3) under frontal collision conditions. Regions A

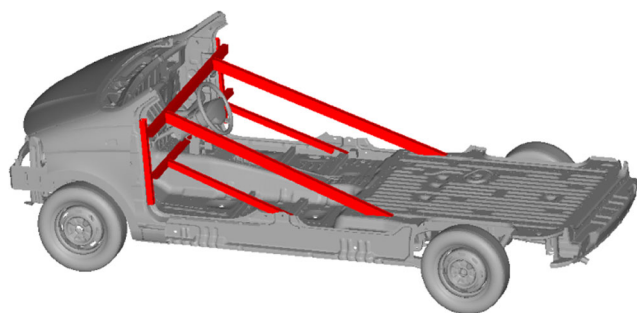


Fig. 11 Final design of the equivalent stents

and B are mainly used to generate relatively stable axial crash deformations and are the main energy absorption regions. Region C relates to engine layout. Because an engine cannot absorb energy during a frontal collision, it is considered a rigid body; thus, region C only acts as a crashing force transmitter. Region D mainly includes the FLB between the back end of the engine and the firewall. The FLB in this region generally absorbs crashing energy via bending deformation during the front-impact process. If the structure in this region is designed to be relatively weak, it will cause the A pillar to move too far backward, thus causing a large intrusion into the firewall and injuring the occupant. The main function of region D is to absorb residual energy and resist excessive bending deformation at the base of the FLB. Therefore, designing a reasonable bending stiffness for region D of the FLB is the key to balancing the two main functions.

3 Parametric modeling of the proposed VRB-VCS FLB structure

A new VRB-VCS FLB structure is proposed based on the conventional UT FLB for more-efficient lightweighting and crashworthiness design. Four improvements are made in this structure relative to the conventional UT FLB: (1) removing the reinforcement plate from the structure to reduce the FLB weight, (2) optimizing the thickness distribution in the FLB inner plate to maximize material utilization, (3) optimizing the FLB cross-sectional geometry to improve the energy absorption and the average crashing force, and (4) optimizing the

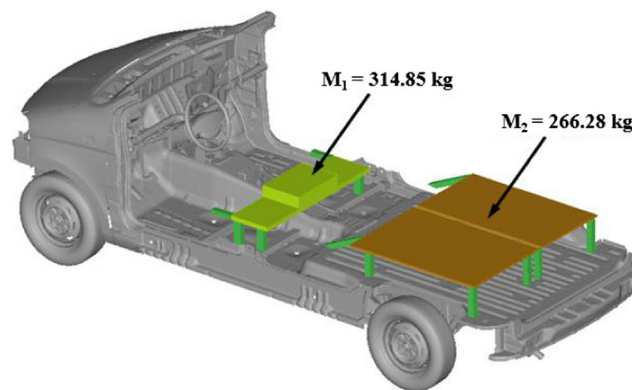


Fig. 12 The deployment locations of counterweights

position and space of the induction structure on FLB for better deformation mode and energy absorption. To optimize the cross-sectional geometry of FLBs, cylindrical notches are used for VRB-VCS FLBs to replace the triggers of the UT FLB, as shown in Fig. 4.

3.1 Parametric modeling of VRB FLB

According to the FLB crash space management method described in Section 2, the VRB FLB is divided into four different functional zones along the direction of rolling in this study. For the VRB FLB structure, the segment with uniform thickness is called constant-thickness zone, and the segment with continuous varying thickness is called as thickness transition zone. Therefore, the aforementioned VRB FLB contains four CTZs and three TTZs, respectively. The VRB FLB thickness distribution parametric model for considering the thickness of the CTZ and the length and position of the TTZ is given in Eq. (1).

$$g(x) = \begin{cases} x_1, & 0 \leq x < x_8 - \frac{1}{2}x_5 \\ x_1 + \frac{x + \frac{1}{2}x_5 - x_8}{x_5}(x_2 - x_1), & x_8 - \frac{1}{2}x_5 \leq x \leq x_8 + \frac{1}{2}x_5 \\ x_2, & x_8 + \frac{1}{2}x_5 < x < x_9 - \frac{1}{2}x_6 \\ x_2 + \frac{x + \frac{1}{2}x_6 - x_9}{x_6}(x_3 - x_2), & x_9 - \frac{1}{2}x_6 \leq x \leq x_9 + \frac{1}{2}x_6 \\ x_3, & x_9 + \frac{1}{2}x_6 < x < x_{10} - \frac{1}{2}x_7 \\ x_3 + \frac{x + \frac{1}{2}x_7 - x_{10}}{x_7}(x_4 - x_3), & x_{10} - \frac{1}{2}x_7 \leq x \leq x_{10} + \frac{1}{2}x_7 \\ x_4, & x_{10} + \frac{1}{2}x_7 < x \leq L \end{cases} \quad (1)$$

where x_1 is the thickness of the first CTZ; x_2 is the thickness of the second CTZ; x_3 is the thickness of the third CTZ; x_4 is the thickness of the fourth CTZ; $x_5, x_6,$ and x_7 are the length of the first, second, and third TTZ, respectively; $x_8, x_9,$ and x_{10} are the position of the first, second, and third TTZ, respectively; x is the distance away from the front end of the VRB FLB structure; and L is the total length of the structure.

The flexible rolling process of VRB is subjected to several manufacturing constraints, e.g., the maximal thickness reduction and the maximal slope which have to be taken into account in the design optimization. Specifically, the following geometric constraints should be considered to ensure the rollability: (1) the transition slopes of the TTZs must vary within 1:100; (2) the ratio between the maximum and minimum thicknesses of the CTZs must vary within 2:1; (3) the sum of $x_5, x_6,$ and x_7 should be less than L ; and (4) the intersection between any two neighboring TTZs must not be occurred, and the TTZs should be distributed within the VRB FLB structure. The mathematical formulation corresponding to the geometric constraints can thus be formulated as

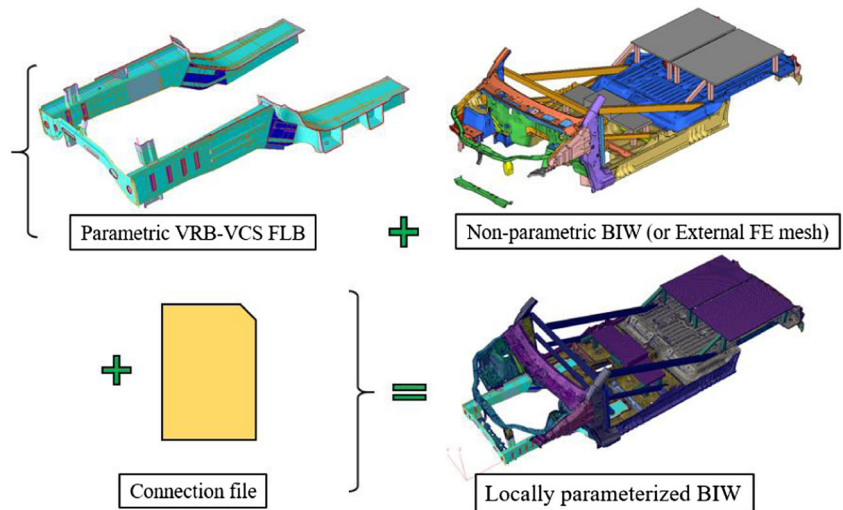
$$\begin{cases} t_{\min} \leq x_1, x_2, x_3, x_4 \leq t_{\max} \\ \max(x_1, x_2, x_3, x_4) \leq 2 \times \min(x_1, x_2, x_3, x_4) \\ x_5 + x_6 + x_7 \leq L \\ \frac{1}{2}x_5 \leq x_8 \leq L - x_6 - x_7 - \frac{1}{2}x_5 \\ x_8 + \frac{1}{2}(x_5 + x_6) \leq x_9 \leq L - x_7 - \frac{1}{2}x_6 \\ x_9 + \frac{1}{2}(x_6 + x_7) \leq x_{10} \leq L - \frac{1}{2}x_7 \end{cases} \quad (2)$$

where t_{\min} and t_{\max} are the minimum and maximum wall thicknesses, respectively.

3.2 Parametric modeling of VCS FLB

In this study, a fully parameterized model of VCS FLB is constructed using SFE-CONCEPT (Hilman et al. 2007;

Fig. 13 Coupling of the parametric model of VRB-VCS FLB and the remaining mesh of BIW



Zimmer 2010; Duan et al. 2017b) which integrates implicit parametrization technique and remeshing algorithm. Because of the implicit definition of the parameters by mapping technology and remeshing algorithm, a flexible and powerful structural geometrical-based cross-sectional shape optimization can be realized. The advantages of the fully parameterized model of VCS FLB are as follows: (1) the high flexibility of the fully parameterized model enables the appropriate and efficient definition of variable cross-sectional shape parameters (Duan et al. 2017b); (2) the adjacent parts, joints, (multi-)flanges, and/or the connections (tied, spotwelds, glue, etc.) follow the geometrical changes during an automated optimization procedure for complex structures via the mapping techniques (Zimmer 2010; Wang and Cai 2017); and (3) high-quality finite element (FE) meshes for larger geometrical changes can be assured via a powerful auto remeshing algorithm, and the simulation accuracy of FE models can thus be assured during the optimization (Cai and Wang 2017b).

The key in the construction of a fully parameterized model for the VCS FLB is the implicit parametrization of the cross-sectional geometry, which is realized here by varying the locations of the control points in the design space of the cross section. Figure 5 shows the implicit parametrization process for the cross-sectional shape of VCS FLBs, in which the z -coordinates of movable points 6–9 are adjusted in the design space of the cross section to parameterize the width of the reinforcement bar, and the y -coordinates of movable points 7 and 8 are varied to parameterize the height. In the same way,

the y -coordinates of movable points 4–11 are adjusted in the design space of the cross section to parameterize the width of the reinforcement bar, and the z -coordinates of the movable points 11 and 12 are adjusted to parameterize the height of the cross section. The corresponding mathematical model of the parametric cross-sectional geometry can be given by

$$\begin{Bmatrix} y_i \\ z_i \end{Bmatrix} = \begin{Bmatrix} y_i^{(\text{initial})} \\ z_i^{(\text{initial})} \end{Bmatrix} + \sum_{j=1}^{n_c} SC_j \begin{Bmatrix} y_i^{(\text{upper})} - y_i^{(\text{initial})} \\ z_i^{(\text{upper})} - z_i^{(\text{initial})} \end{Bmatrix} \quad (3)$$

where the subscript i denotes the control point number of cross-sectional shape; the superscripts “initial” and “upper” refer to the initial position and upper bound of control points, respectively; n_c is the number of cross-sectional shape parameters; SC_j is the scale factor of the j th cross-sectional shape parameter; and y_i and z_i are the coordinate values in the local coordinate system of the i th control point, respectively.

The corresponding control equation for cross-sectional shape parameter can be expressed as

$$x_j = x_j^{(\text{initial})} + \sum_{j=1}^{n_c} SC_j (x_j^{(\text{upper})} - x_j^{(\text{initial})}) \quad (4)$$

where x_j is the parameter of the j th cross-sectional shape, $x_j^{(\text{initial})}$ is the initial value of x_j , and $x_j^{(\text{upper})}$ is the upper bound of x_j .

The cross-sectional shape of a VCS FLB cannot be altered arbitrarily. It must satisfy stamping constraints, such as the

Fig. 14 Assembly process for the local parametric subsystem front-impact model

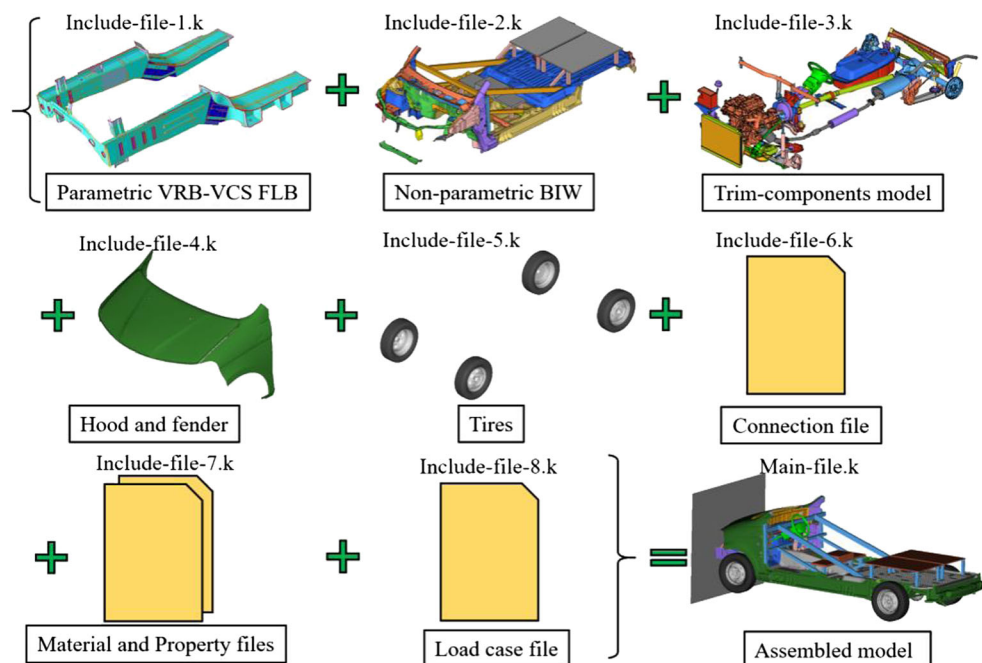
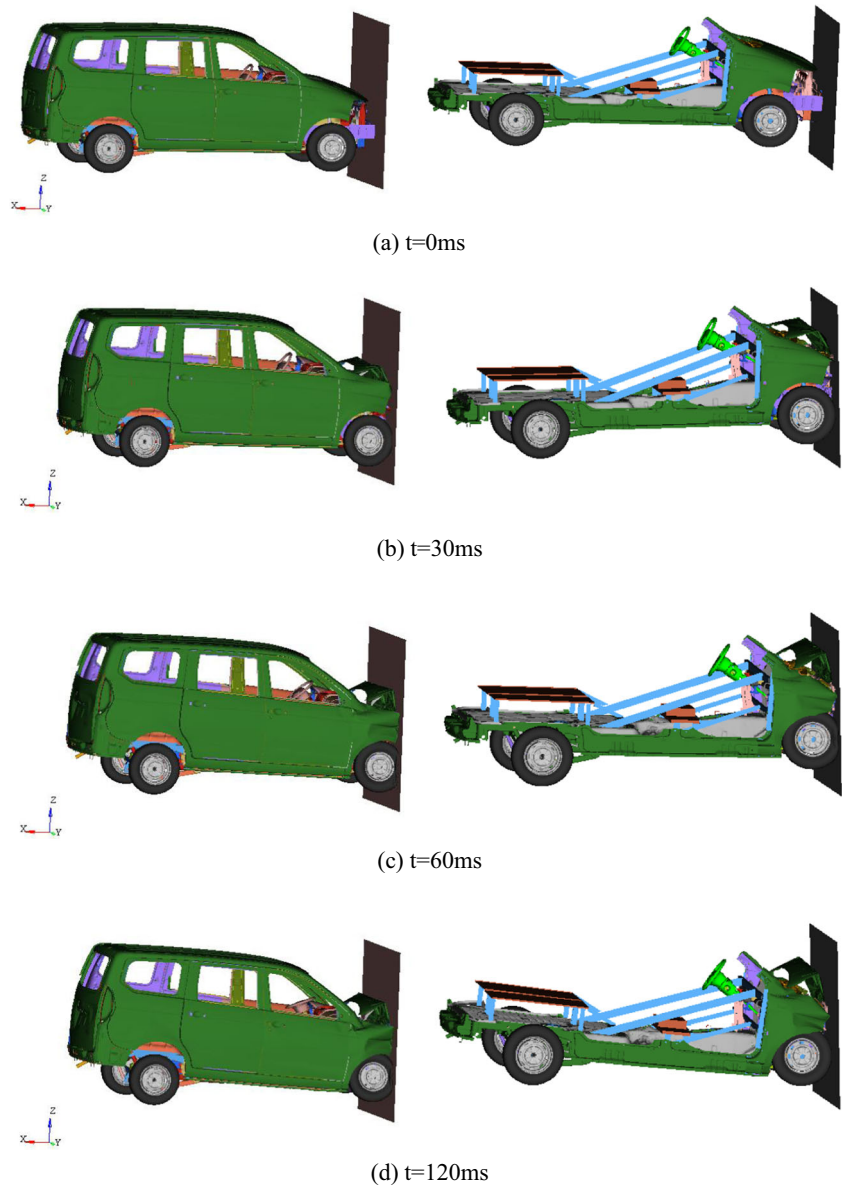


Fig. 15 Comparison of the deformation patterns between the full-scale vehicle model and the local parametric subsystem front-impact model. **a** $t = 0$ ms. **b** $t = 30$ ms. **c** $t = 60$ ms. **d** $t = 120$ ms



prohibition of negative angles or intersections, as shown in Fig. 6. Based on these constraints, a mathematical model of stamping constraints for a VCS FLB is constructed.

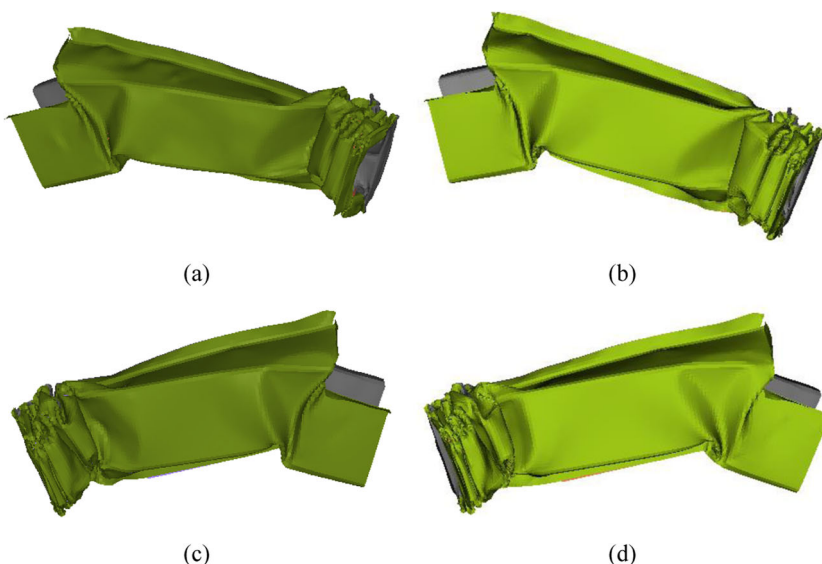
$$\begin{cases} \alpha_i \geq \alpha_{allowable} \\ W_i \geq W_{allowable} \\ H_i \leq H_{allowable} \\ n_{overlap} = 0 \end{cases} \quad (5)$$

where α_i is the draft angle; W_i is the width of FLB bead; H_i is the height of FLB bead; $\alpha_{allowable}$ and $W_{allowable}$ are the specified lower bound of the draft angle and the width of FLB bead, respectively; $H_{allowable}$ is the specified upper bound of the height of FLB bead; and $n_{overlap}$ is the number of intersection points.

3.3 Parametric modeling of VRB-VCS FLB

The steel grade of the VRB-VCS FLB is HSLA340, whose Young's modulus, Poisson's ratio, and density are 210 GPa, 0.3, and $7.83 \times 10^3 \text{ kg/m}^3$, respectively. From the flexible rolling process of VRB (see Fig. 1), there are different material properties for individual part with different thicknesses. Therefore, the variable thicknesses and non-uniform material properties in different local zones have to be considered in the FE model of the VRB-VCS FLB structure. However, it is difficult for existing commercial software to establish variable thicknesses and material properties simultaneously. To construct a parametric model for a VRB-VCS FLB structure, we compiled a VRB FLB thickness distribution parametric model as well as an efficient mapping algorithm for the material

Fig. 16 Comparison of the deformation patterns of FLB. **a** Left FLB of full-scale vehicle. **b** Left FLB of subsystem model. **c** Right FLB of full-scale vehicle. **d** Right FLB of subsystem model



parameters and element node thicknesses of the VCS FLB implicit parametric model. The general procedure of the proposed method is described by the following steps:

- Step 1: Write a corresponding MATLAB program according to the VRB FLB thickness distribution parametric model in Section 3.1.
- Step 2: Use MATLAB call SFE-CONCEPT software to convert the VCS FLB implicit parametric model into a corresponding FE model.
- Step 3: Read information on nodes and elements from the FE model of VCS FLB using MATLAB code.
- Step 4: Sort the FE grid nodes of the VCS FLB by their coordinate values along the rolling direction and assign the thickness information of the VRB FLB parametric model along the rolling direction to all nodes on the shell elements of the VCS FLB FE model. The shell elements with variable thickness is modeled by using the keyword *ELEMENT_SHELL_THICKNESS in LS-DYNA (Halquist 2007), as shown in Fig. 8, where $n_1 \sim n_4$ represent nodal point 1~nodal point 4, respectively,

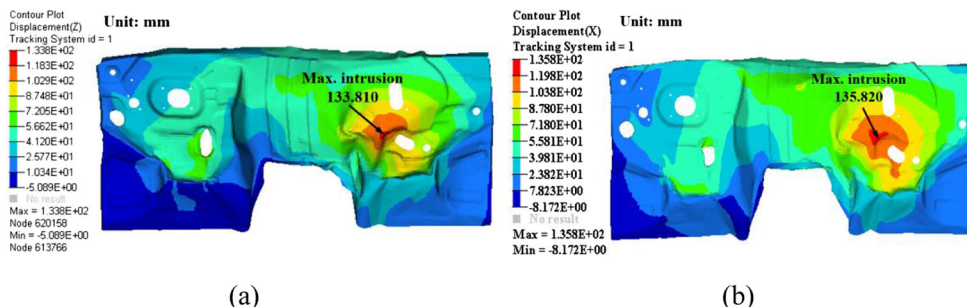
and thick 1~thick 4 represent the shell thickness at node 1~node 4, respectively.

- Step 5: To model the variable material properties of the VRB-VCS FLB structure, the elements with nearly the same thickness are defined as one component. Each component is assigned with its own mechanical properties which are obtained from the effective stress vs. effective plastic strain field established by Duan et al. (Duan et al. 2016). Since the high-strength steel grade HSLA340 is strain rate sensitive, the strain rate effect must be taken into account in the analysis. The effect is accounted through the Cowper-Symonds model (Halquist 2007; Alves 2000) given as

$$\sigma_y = \sigma_0 \left[1 + \left(\frac{\dot{\epsilon}}{C} \right)^{\frac{1}{P}} \right] \tag{6}$$

where $\dot{\epsilon}$ is the strain rate, σ_0 is the yield strength, σ_y is the scaled yield strength, and C and P are the strain rate parameters, respectively. In this paper, the parameter $C = 0.04$ and $P = 5$ are used.

Fig. 17 Comparison of the dash panel intrusion contours. **a** Full-scale vehicle. **b** Subsystem model



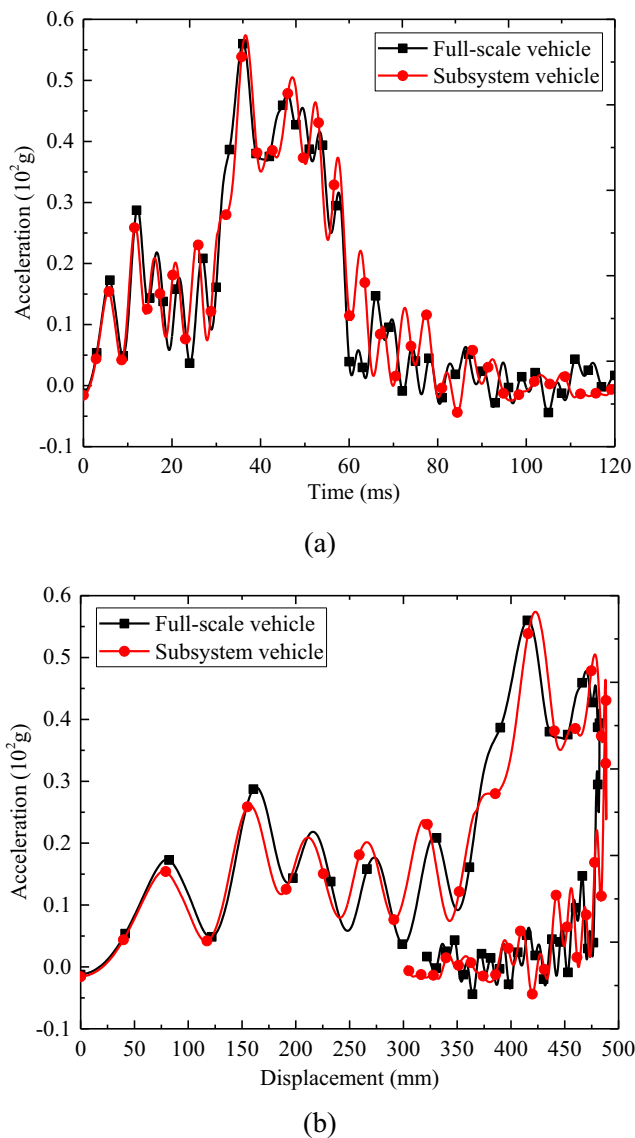


Fig. 18 Comparison of the crash pulses on the left sill at B pillar. **a** Acceleration vs. time curve. **b** Acceleration vs. displacement curve

Step 6: Export the new established FE model of the VRB-VCS FLB structure with variable thicknesses and material properties.

The VRB-VCS FLB parametric model can be obtained by executing these steps. The FE model of the VRB-VCS FLB structure is shown in Fig. 7.

4 Multiobjective crashworthiness optimization of VRB-VCS FLB

Achieving crashworthiness and lightweightness in FLBs at the same time is very difficult. It seems that combinations of variable wall thickness and variable cross-sectional shape optimization may be a promising way.

However, the design complexity is increased due to the following three factors: fully parameterized model of VRB-VCS FLB (automated creation of high-quality FE meshes for larger geometrical changes), high computational cost (a large number of FE simulations and function evaluations), and low efficiency of data processing. In order to improve computational efficiency, an efficient design strategy is proposed in this paper to reduce complexity and to conduct the multiobjective crashworthiness optimization. The proposed method consists of three major parts. Firstly, a fully parameterized model of VRB-VCS FLB is established, which is prerequisite for variable wall thickness and variable cross-sectional shape optimization. Secondly, a local parametric subsystem front-impact model is constructed to improve the updating efficiency of FE model for design points, as well as to reduce their computation time. Finally, a fully automated design of experiment (DOE) platform is established to improve the efficiency of data collection, and epsilon-support vector regression technique and non-dominated sorting genetic algorithm II were utilized to search the Pareto optimal frontier. An overview of the proposed design strategy is shown in Fig. 8. And, the following sections describe the method in details.

4.1 Constructing a local parametric subsystem front-impact model

To improve computational efficiency, this study used a verified full-scale vehicle front-impact model as a foundation and established a local parametric subsystem front-impact model that balances accuracy and efficiency. This section mainly discusses three topics: subsystem model extraction, construction of the local parametric subsystem front-impact model, and model verification.

4.1.1 Subsystem model extraction

Energy absorption analysis To reasonably extract the critical crashing energy-absorbing components, an energy absorption analysis must be performed on the full-scale vehicle front-impact simulation results. Figure 9 shows the several important crashing energy absorption components. In order of their importance to energy absorption, the FLB is first, followed by the front bumper beam, subframe, and center longitudinal beam. These key energy-absorbing components should be preserved in the subsystem model to ensure the accuracy of the subsystem front-impact model.

Component selection This paper discusses a front engine and rear-wheel drive vehicle. During a collision, the engine, transmission, and drive shaft will suffer heavy

Table 1 Error analysis of the local parametric subsystem front-impact model

Indicators	Full-scale vehicle model	Subsystem model	Error (%)
Peak acceleration (g)	56.01	57.39	2.46
Occurrence time of peak acceleration (ms)	36.09	36.64	1.52
Dash panel intrusion (mm)	133.81	135.82	1.50
Maximum dynamic intrusion of vehicle (mm)	482.29	488.61	1.31

longitudinal crashing forces. These crashing forces are transmitted through the paths of the FLB in the following order: shotgun, subframe toward the engine, transmission, steering system, under body structure, drive shaft, exhaust system, tank, and rear tires. To reflect the subsystem model movement states during the collision, the front and rear tires and the front and rear suspension systems should be considered key components and should be retained. Therefore, the subsystem model is composed of key energy absorption components and important mechanical transmission structures (Fig. 10).

Establishment of equivalent stents Equivalent stents are added to the subsystem and are mainly used to simulate the subsystem model movement state and dynamic response of the car body. When establishing the equivalent stents, the car body deformation and crashing force transmission path should both be considered. The structure and installation positions of the equivalent stents are continuously adjusted based on engineering experience and impact simulation results to make the crashing force transmission and deformation mode of subsystem almost identical to the full-scale vehicle collision model. Figure 11 shows the final design of the equivalent stents.

Model counterweight The vehicle curb weight affects the initial kinetic energy of the impact model; thus, an additional counterweight must to be added to the subsystem model to achieve the same initial kinetic energy as in the full-scale vehicle impact model. The center of mass location will affect the motion state of the impact model. Therefore, the consistency between the center of mass location and the curb weight (both 1350 kg) of the subsystem model and the full-scale vehicle model should be reasonably ensured when counterweighting. Figure 12 shows the weights and deployment locations of the counterweights in the subsystem model.

4.1.2 Constructing the local parametric subsystem front-impact model

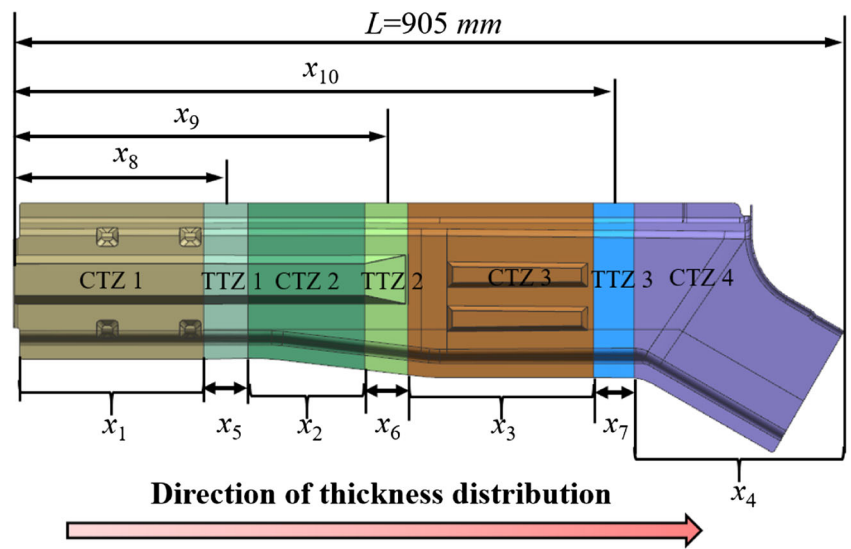
This section establishes the local parametric subsystem front-impact model. This model is composed of a full parametric VRB-VCS FLB assembly model and a non-parametric FE model. The greatest advantage of this model is that changing the VRB-VCS FLB structure thickness distribution and cross-sectional shape does not affect the non-parametric FE model; that is, the non-parametric FE model remains fixed during the optimization process. The detailed procedure to establishing the local parametric subsystem front-impact model is given in following steps:

- Step 1: Divide the FE mesh of body-in-white (BIW) established in Section 4.1.1 into two parts: the first part contains the mesh of VRB-VCS FLB, while the second part contains the remaining mesh of BIW.
- Step 2: Establish a parametric model of VRB-VCS FLB by using the method proposed in Section 3 and replace the original VRB-VCS FLB with the parametric model of VRB-VCS FLB.
- Step 3: Embed the parametric model of VRB-VCS FLB into the non-parametric FE model of BIW: special connection scripts are used here to connect the parametric model of VRB-VCS FLB for the remaining FE model of BIW (i.e., non-parametric FE model of BIW). The interface between the parametric model of VRB-VCS FLB and the remaining FE model of BIW is located at the sections where the VRB-VCS FLB model is cut out from the BIW. The schematic of aforementioned coupling is shown in Fig. 13.
- Step 4: Assemble the parametric model of VRB-VCS FLB and the non-parametric FE models: for components, e.g., non-parametric BIW, engine, suspension and tires, that were not changed during optimization are

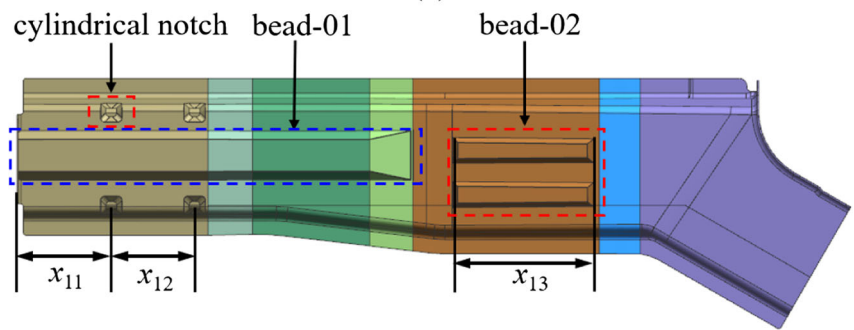
Table 2 Differences between the full-scale vehicle model and the subsystem model

	Full-scale vehicle model	Subsystem model	Rate of change (%)
Number of elements	972,074	664,694	- 31.62
Number of nodes	1,004,414	678,922	- 32.41
Number of spotwelds	6063	3623	- 40.24
Computation time (h)	12.2	6.5	- 46.72

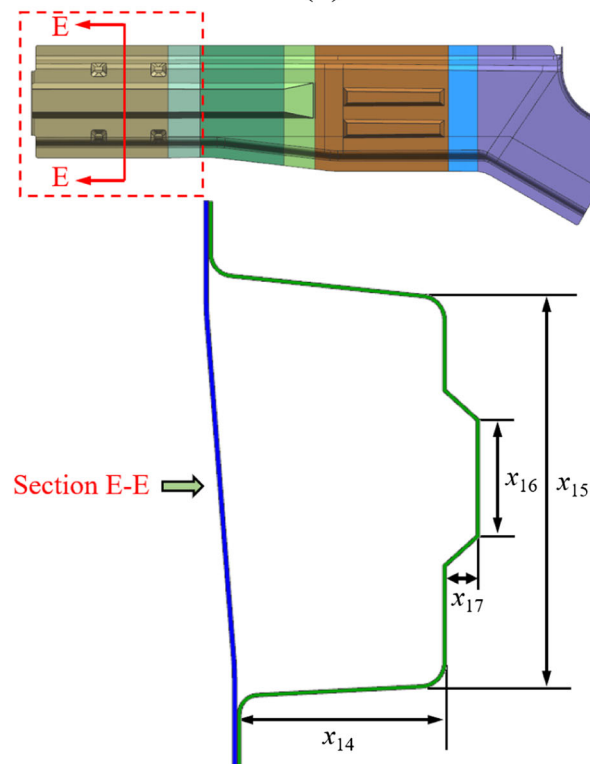
Fig. 19 Illustration of design variables. **a** Thickness distribution variables. **b** Topology variables. **c** Cross-sectional shape variables



(a)



(b)



(c)

Table 3 Description of design variables (unit: mm)

Variable name	Symbol	Lower bound	Upper bound	Baseline design
Thickness of CTZ 1	x_1	1.0	2.4	1.6
Thickness of CTZ 2	x_2	1.0	2.4	1.6
Thickness of CTZ 3	x_3	1.0	2.4	1.6
Thickness of CTZ 4	x_4	1.0	2.4	1.6
Length of TTZ 1	x_5	$100 \times (x_2 - x_1)$	140.0	40.0
Length of TTZ2	x_6	$100 \times (x_3 - x_2)$	140.0	40.0
Length of TTZ 3	x_7	$100 \times (x_4 - x_3)$	140.0	40.0
Position of TTZ 1	x_8	150.0	260.0	230.0
Position of TTZ 2	x_9	330.0	410.0	370.0
Position of TTZ 3	x_{10}	570.0	690.0	650.0
Position of the first cylindrical notch	x_{11}	50	100.0	85.0
Distance between the cylindrical notches	x_{12}	50	120.0	90.0
Length of bead 02	x_{13}	0	160.0	0.0
Width of cross section	x_{14}	60.0	95.0	81.0
Height of cross section	x_{15}	100.0	140.0	115.0
Width of bead 01	x_{16}	25.0	60.0	40.0
Height of bead 01	x_{17}	-14.0	14.0	0.0

meshed as separate FE model files. The interface attachments between the BIW and those components are defined and linked through rigid patches. Using the include-file structure of LS_DYNA, all the finite element analysis (FEA) contents including load case, non-parametric BIW, trim component model, hood, and tires are kept in include-files. Those include-files and the file containing the parametric model of VRB-VCS FLB can be automatically assembled with no additional user intervention. The assembly process of establishing the local parametric subsystem front-impact model is shown in Fig. 14.

4.1.3 Model verification

In accordance with specifications in *The Protection of The Occupants in The Event of a Frontal Collision for Motor Vehicle* (GB 11551-2003), this study used an initial speed of 50 km/h and undertook a full-width front-impact simulation using the full-scale vehicle and local parametric subsystem models. The following will verify the simulation accuracy and efficiency of the local parametric subsystem front-impact model from the aspects of deformation mode, firewall intrusion, and acceleration curve. A comparison of the global deformation history of the full-scale vehicle and local parametric subsystem front-impact models is shown in Fig. 15.

Figure 15 shows that during the impact process, the front end structures of both the full-scale vehicle and local

parametric subsystem front-impact models suffer severe deformation; both the hood and the fender produce similar bending deformations. The front end structure crashing degrees and the rising degrees of the rear under bodies of the two models are consistent, and the passenger cabin is basically undeformed. These results indicate that the global deformations on the full-scale vehicle and the local parametric subsystem front-impact models are quite consistent.

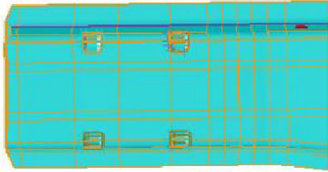
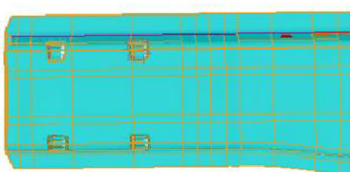
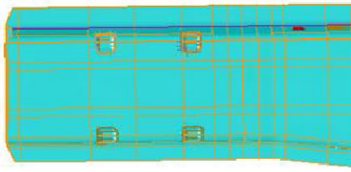
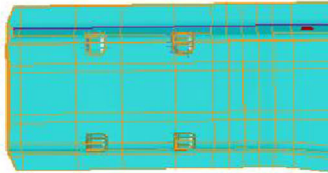
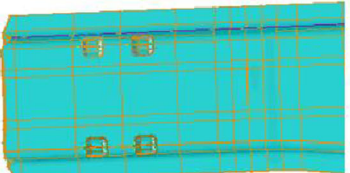
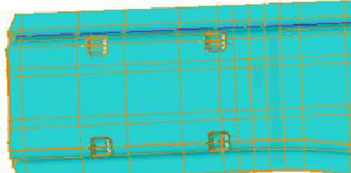
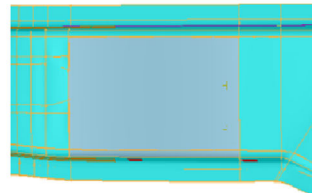
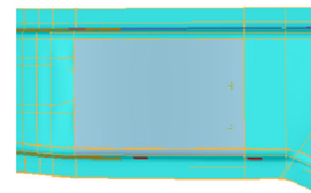
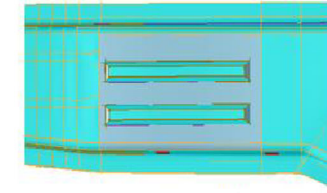
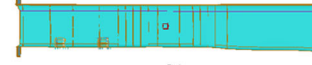
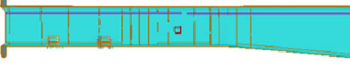
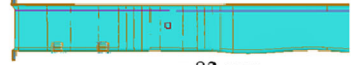
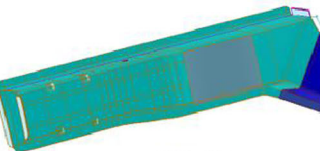


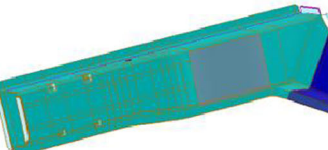
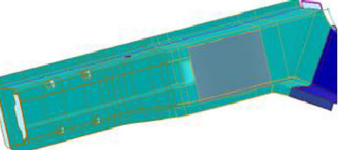

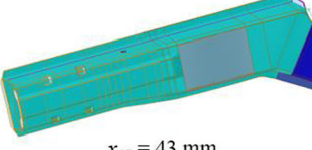
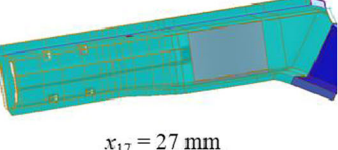
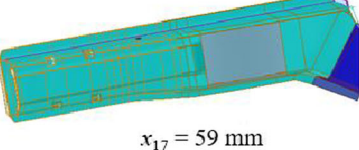
Figure 16 shows the left and right FLB deformation modes of the full-scale vehicle and local parametric subsystem front-impact models. The left and right FLB deformation modes of the two models are quite similar; both have crashing and then bending in the front half region of the beam, and similar bending deformations occur at the kickdown location.

Figure 17 compares the firewall intrusions from the full-scale vehicle and local parametric subsystem front-impact models. The firewall deformation modes of the two models are quite similar. The error between the firewall intrusions of the local parametric subsystem front-impact model relative to that of the full-scale vehicle impact model is controllable within 3%. Thus, the local parametric subsystem front-impact model accurately reflects the intrusion variation of the full-scale vehicle impact model.

Figure 18 compares the acceleration curves from the full-scale vehicle and local parametric subsystem front-impact models. The acceleration curves of the full-scale vehicle and local parametric subsystem front-impact models are in good agreement; the peak values and occurrence time are consistent between the two models.

Table 1 lists the FE results of the full-scale vehicle impact model and the local parametric subsystem front-impact model.

Table 4 Geometric characteristics of the VRB-VCS FLB with different variable values

Baseline design	Lower bound	Upper bound
 $x_{11} = 85 \text{ mm}$	 $x_{11} = 50 \text{ mm}$	 $x_{11} = 100 \text{ mm}$
 $x_{12} = 92 \text{ mm}$	 $x_{12} = 50 \text{ mm}$	 $x_{12} = 120 \text{ mm}$
 $x_{13} = 0 \text{ mm}$	 $x_{13} = 0 \text{ mm}$	 $x_{13} = 160 \text{ mm}$
 $x_{14} = 81 \text{ mm}$	 $x_{14} = 70 \text{ mm}$	 $x_{14} = 92 \text{ mm}$
 $x_{15} = 118 \text{ mm}$	 $x_{15} = 100 \text{ mm}$	 $x_{15} = 140 \text{ mm}$
 $x_{16} = 0 \text{ mm}$	 $x_{16} = -14 \text{ mm}$	 $x_{16} = +14 \text{ mm}$
 $x_{17} = 43 \text{ mm}$	 $x_{17} = 27 \text{ mm}$	 $x_{17} = 59 \text{ mm}$

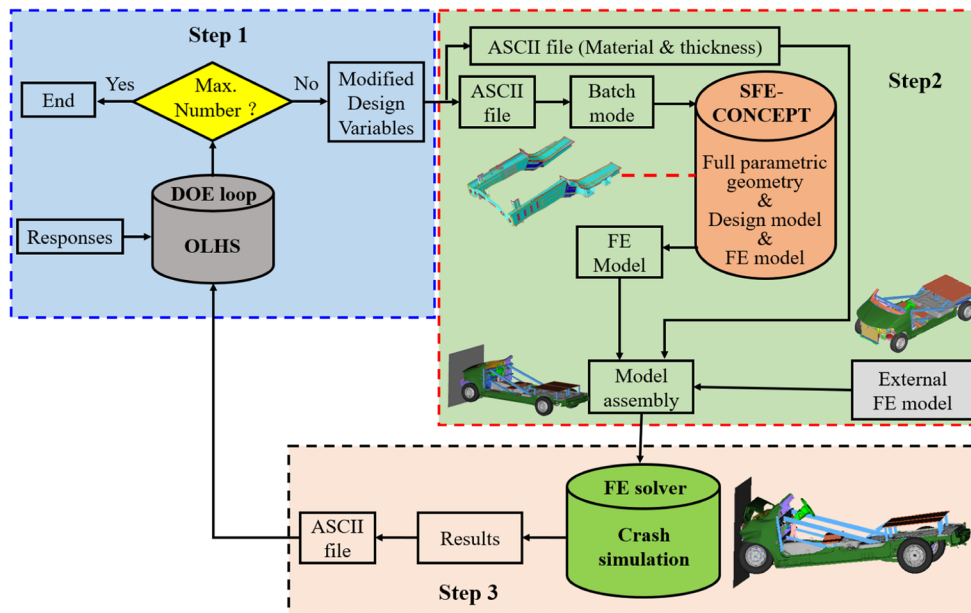
It is revealed by comparison with the full-scale vehicle impact model that the accuracy of the local parametric subsystem front impact model is controllable within 3%.

Table 2 lists the differences between the full-scale vehicle impact model and the local parametric subsystem front-impact model. When compared with the full-scale vehicle model, the local parametric subsystem front-impact model reduces the

element number by 31.62%, the node number by 32.41%, and the spotweld number by 40.24%. In addition, the calculation time for the local parametric subsystem front-impact model is 46.72% shorter than that of the full-scale vehicle impact model.

In summary, to guarantee simulation accuracy, the local parametric subsystem front-impact model can reduce the

Fig. 20 Fully automated implementation platform in the DOE loop



calculation time by 46.72% when compared with that of the full-scale vehicle impact model, which greatly improves the crash simulation analysis efficiency. Therefore, the local parametric subsystem front-impact model can replace the full-scale vehicle impact model in subsequent optimizations.

4.2 Design responses and variables

Crash pulse is one of the most significant factors to describe vehicle crash behavior, which can be simplified as a two-step crash pulse for the vehicle with front engine. Therefore, the two-step crash pulse is adopted in this study to quantify the actual crash pulse curve with few parameters such as the first-step acceleration (G_1) and the second-step acceleration (G_2). Generally, the larger the value of G_1 and the smaller the value of G_2 , the better the occupant protection response (Duan et al. 2016). Besides, the weight of VRB-VCS FLB, the peak acceleration of crash pulse, the energy absorption of VRB-VCS FLB, and the dash panel intrusion are also chosen as the crashworthiness indicators, and they are represented by $M(x)$, $A(x)$, $E(x)$, and $S(x)$, respectively.

Table 5 Accuracy assessment for the ϵ -SVR models

	R^2	RAAE	RMAE
$M(x)$	0.9990	0.0301	3.1152
$A(x)$	0.9742	0.2030	1.1877
$G_1(x)$	0.9931	0.0952	1.0746
$G_2(x)$	0.9846	0.1574	1.1133
$E(x)$	0.9827	0.1571	1.2080
$S(x)$	0.9616	0.2120	1.2354

In this paper, the selection of design variables is based on design requirements, engineering judgment, and the number of design parameters (optimization time). Specifically, 17 design variables including 10 thickness distribution variables, 3 topology variables, and 4 cross-sectional shape variables are defined in the parametric model of VRB-VCS FLB, as shown in Fig. 19. The 17 variables can be grouped into three sets: x_1 to x_{10} are thickness distribution variables, x_{11} to x_{13} are topology variables, and x_{14} to x_{17} are cross-sectional shape variables. The details of the design variables are listed in Table 3. To illustrate visually, the geometric characteristic changes of the VRB-VCS FLB structures are compared in Table 4 under selection of the baseline and extreme values for the design variables.

In Fig. 19, section E-E represents the cross section of CTZ 1 and TTZ 1.

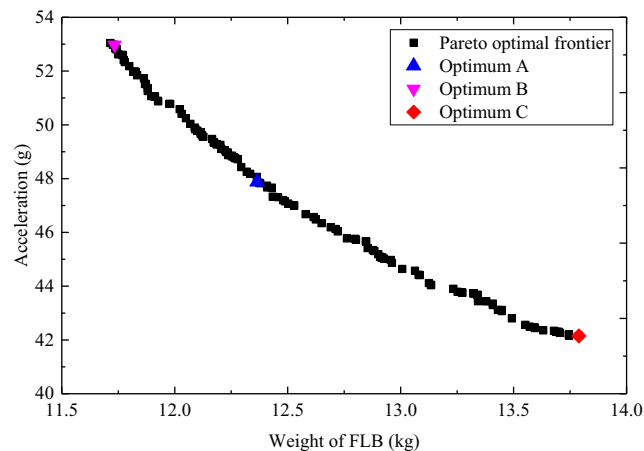


Fig. 21 Pareto optimal frontier for the MOO problem

Table 6 Comparison of the design parameters between baseline and optimal designs

Symbol	Baseline design	Optimum A	Optimum B	Optimum C
x_1	1.600	1.859	1.860	1.968
x_2	1.600	2.236	2.167	2.397
x_3	1.600	1.647	1.635	2.026
x_4	1.600	1.715	1.463	2.248
x_5	40.000	56.695	62.045	58.022
x_6	40.000	64.470	68.618	64.499
x_7	40.000	46.327	40.657	45.645
x_8	230.000	242.753	240.084	241.37
x_9	370.000	407.052	404.338	409.465
x_{10}	650.000	658.173	658.301	659.984
x_{11}	85.000	87.319	88.029	85.485
x_{12}	90.000	91.251	91.250	91.251
x_{13}	0.000	147.898	150.047	141.796
x_{14}	81.000	71.464	62.575	73.690
x_{15}	115.000	118.374	119.926	119.763
x_{16}	40.000	41.725	42.632	42.787
x_{17}	0.000	-8.207	-5.651	-8.746

4.3 Optimization problem setup

It should be noted that peak acceleration of crash pulse $A(x)$ is one of the most significant factors to indicate the safety of occupants. A large peak acceleration may cause severe injury or even death. For this reason, the peak acceleration of crash pulse should be minimized. The weight of the VRB-VCS FLB $M(x)$ is also an important indicator of the cost of energy absorber. It is employed as the other objective functions and should be minimized. The performances of $G_1(x)$, $G_2(x)$, $E(x)$, and $S(x)$ are

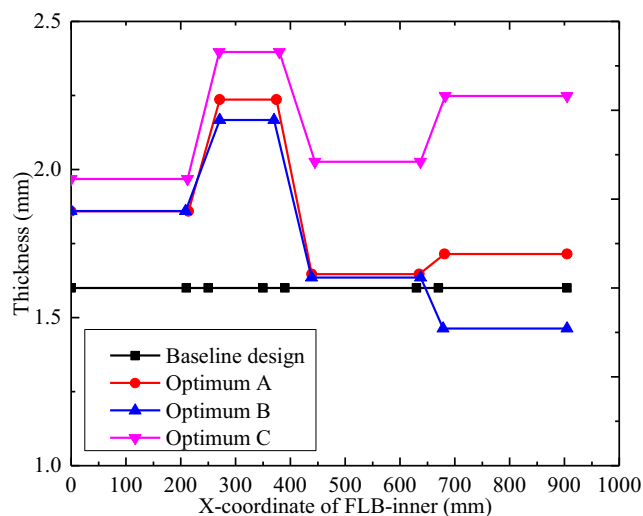


Fig. 22 Comparison of the thickness distributions of the optimized VRB-VCS FLB-inners and the UT FLB-inner counterpart

selected as the constraint functions. Considering real requirements, the multiobjective optimization (MOO) model for the lightweightness and crashworthiness design of VRB-VCS FLB can be formulated as

$$\begin{cases} \min & \{M(x), A(x)\} \\ \text{s.t.} & G_1(x) \geq 15 \\ & G_2(x) \leq 43 \\ & E(x) \geq 62,000 \\ & S(x) \leq 130 \\ & 1 \leq x_1, x_2, x_3, x_4 \leq 2.4 \\ & \max(x_1, x_2, x_3, x_4) \leq 2 \times \min(x_1, x_2, x_3, x_4) \\ & x_5 + x_6 + x_7 \leq 905 \\ & \frac{1}{2}x_5 \leq x_8 \leq 905 - x_6 - x_7 - \frac{1}{2}x_5 \\ & x_8 + \frac{1}{2}(x_5 + x_6) \leq x_9 \leq 905 - x_7 - \frac{1}{2}x_6 \\ & x_9 + \frac{1}{2}(x_6 + x_7) \leq x_{10} \leq 905 - \frac{1}{2}x_7 \\ & 50 \leq x_{11} \leq 100, 50 \leq x_{12} \leq 120, 0 \leq x_{13} \leq 160 \\ & 60 \leq x_{14} \leq 95, 100 \leq x_{15} \leq 140, 25 \leq x_{16} \leq 60, -14 \leq x_{17} \leq 14 \\ & x = (x_1, x_2, x_3, x_4, x_5, x_6, x_7, x_8, x_9, x_{10}, x_{11}, x_{12}, x_{13}, x_{14}, x_{15}, x_{16}, x_{17})^T \end{cases} \tag{7}$$

4.4 Constructing a fully automated design of experiment platform

In order to obtain the underlying relationship between the design variables and the sophisticated responses, sample points are needed to explore the design space by using DOE. Among the many experimental design methods, the optimal Latin hypercube sampling (OLHS) (JS P 1994; Shields and Zhang 2016) is considered to perform DOE due to its high efficiency. The OLHS algorithm combines the advantages of LHS and optimal design, so that the sample points are more uniformly distributed in the whole design space. Therefore, the OLHS method is adopted to sampling samples in this paper.

The DOE procedure for VRB-VCS FLB mainly includes sampling of samples, updating simulation model, numerical simulation analysis, and postprocessing. As the number of sample points increases, the computational burden for updating the subsystem front-impact model and postprocessing is very huge, which caused the DOE procedure for VRB-VCS FLB to become very time consuming. To address the aforementioned problem, establishing a fully automated DOE platform is very important for improving the efficiency of data collection. We used MATLAB to integrate the stages of sampling for samples, simulation model update, numerical simulation analysis, and postprocessing. A fully automated DOE platform is constructed to greatly improve experimental design efficiency. The details of the procedure are shown in Fig. 20 and given in the following steps:

- Step 1: OLHS is adopted for sampling the design variables. In this study, 1000 sample points are generated according to the geometrical constraints of the

Fig. 23 Comparison of the cross-sectional shape changes of the optimized VRB-VCS FLB structures and the UT FLB counterpart. **a** Baseline design. **b** Optimum A. **c** Optimum B. **d** Optimum C

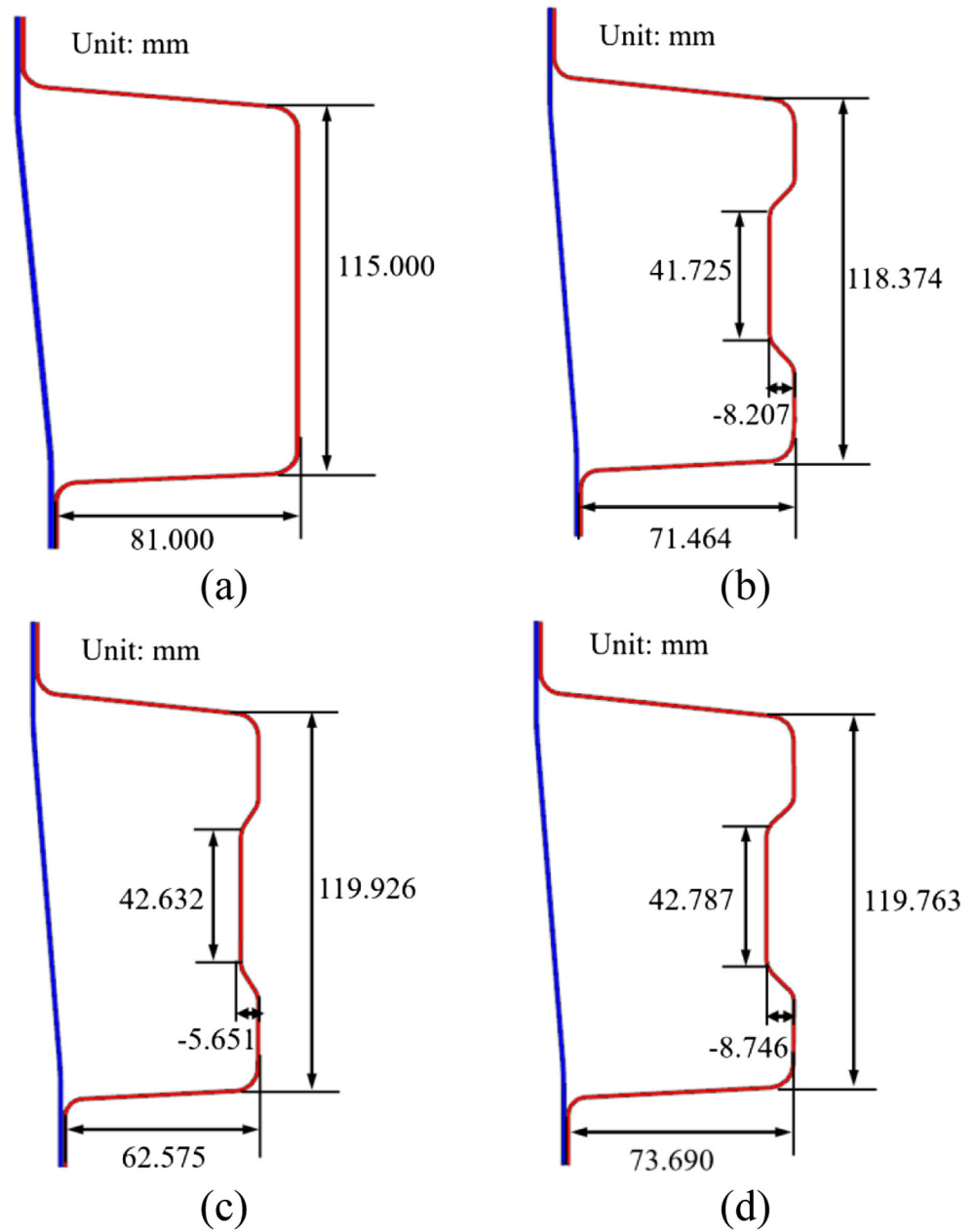


Fig. 24 Comparison of the structural characteristics of the optimized VRB-VCS FLBs and the UT FLB counterpart. **a** Baseline design. **b** Optimum A. **c** Optimum B. **d** Optimum C

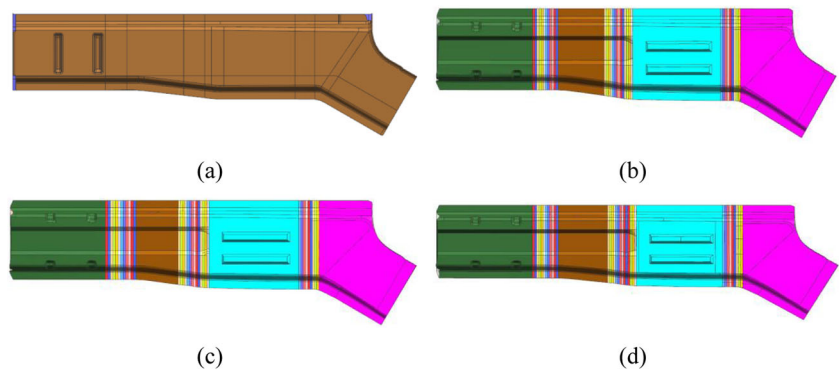


Table 7 Comparison of the optimal solutions between FEA and approximate values

Description	Symbol	FEA	ϵ -SVR	Error (%)
Optimum A	$M(x)$	12.410 (kg)	12.365 (kg)	-0.363
	$A(x)$	48.570 (g)	47.879 (g)	-1.422
	$G_1(x)$	18.180 (g)	18.791 (g)	3.361
	$G_2(x)$	40.240 (g)	41.434 (g)	2.967
	$E(x)$	65,348.900 (J)	66,579.100 (J)	1.882
	$S(x)$	128.400 (mm)	129.977 (mm)	1.228
Optimum B	$M(x)$	11.814 (kg)	11.734 (kg)	-0.677
	$A(x)$	54.612 (g)	52.974 (g)	-2.999
	$G_1(x)$	16.820 (g)	17.218 (g)	2.366
	$G_2(x)$	42.310 (g)	42.928 (g)	1.461
	$E(x)$	62,267.500 (J)	63,251.900 (J)	1.581
	$S(x)$	127.500 (mm)	129.697 (mm)	1.723
Optimum C	$M(x)$	13.911 (kg)	13.789 (kg)	-0.977
	$A(x)$	43.189 (g)	42.151 (g)	-2.403
	$G_1(x)$	21.140 (g)	21.790 (g)	3.075
	$G_2(x)$	39.090 (g)	38.144 (g)	2.420
	$E(x)$	71,748.521 (J)	72,830.213 (J)	1.508
	$S(x)$	127.400 (mm)	129.043 (mm)	1.290

optimization formulation (Eq. (7)) for the VRB-VCS FLB structure.

Step 2: The commercial software programs SFE-CONCEPT and LS_DYNA are integrated by MATLAB code. The design geometry of the VRB-VCS FLB is updated and meshed in SFE-CONCEPT. The FE model of the VRB-VCS FLB is exported in LS_DYNA format and automatically assembled with several non-parametric FE models such as BIW, trim component model, hood, and tires. The local parametric subsystem front-impact model with the parameters of the current sample point is then updated in this step.

Step 3: The objectives and constraint values of the current sample point are solved explicitly using the

commercial software LS_DYNA. Once the FEA is completed, the results will be automatically read by MATLAB.

Step 4: In the DOE loop, variations of the shape and thickness parameters are recorded in SFE-CONCEPT. The OLHS with MATLAB code is utilized to control the SFE-CONCEPT to output an updated subsystem front-impact model with another set of parameters. This cycle restarts until the maximum number of sample points is reached.

4.5 Construction of surrogate model

The surrogate model-based methods have been widely adopted to improve computational efficiency for large-scale engineering problems (Xiao et al. 2014, 2018a, b). As an effective alternative, epsilon support vector regression (ϵ -SVR), which is a promising metamodeling technique for function approximation of vehicle crash problems (Duan et al. 2017a; Duan et al. 2016; Clarke et al. 2005; Song et al. 2013), is utilized to construct metamodels of the sophisticated output responses (i.e., $M(x)$, $A(x)$, $G_1(x)$, $G_2(x)$, $E(x)$, $S(x)$).

The decision function of ϵ -SVR can be written as

$$f(x) = \sum_{i=1}^l \left(\bar{\alpha}_i^* - \bar{\alpha}_i \right) k(x_i, x) + \bar{b} \tag{8}$$

where l is the number of training samples, x_i is the i th training sample, and $\bar{\alpha}_i$ and $\bar{\alpha}_i^*$ are Lagrange multipliers, and the parameter \bar{b} can be formulated as

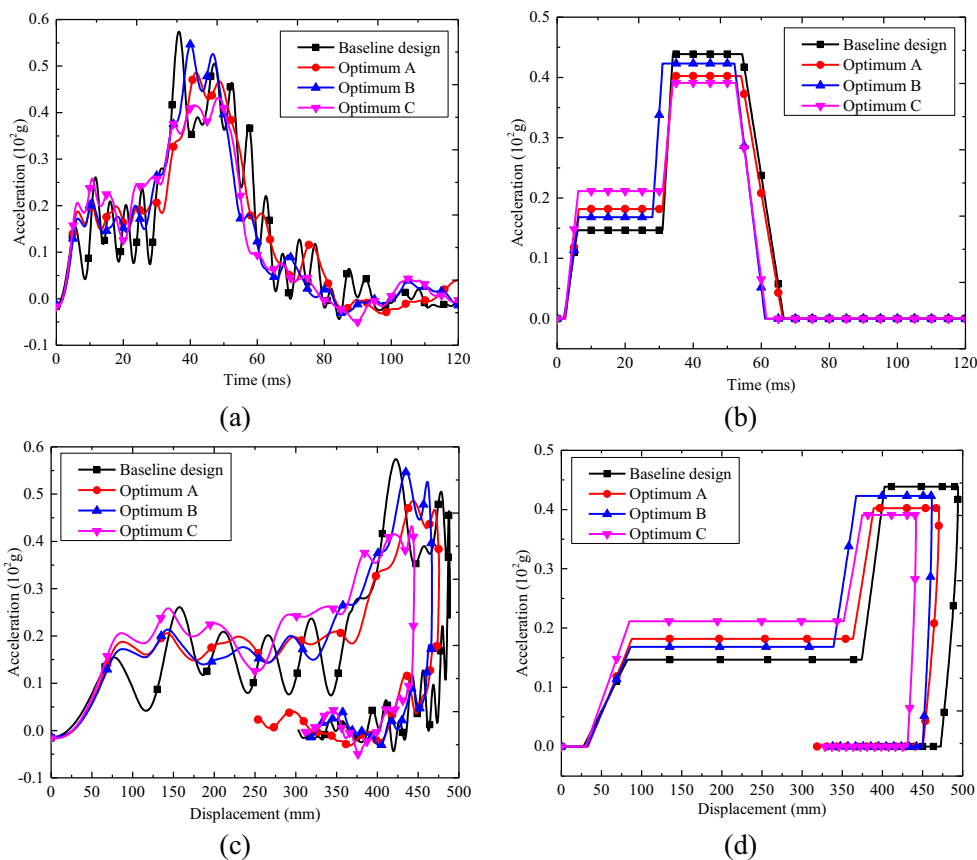
$$\bar{b} = y_j - \sum_{i=1}^l \left(\bar{\alpha}_i^* - \bar{\alpha}_i \right) k(x_i, x_j) + \epsilon, \forall j \in \{j | 0 < \bar{\alpha}_j < C\} \tag{9}$$

where y_j is the target output of the i th training sample, $C > 0$ is the penalty factor of error term, $\epsilon > 0$ is the insensitive loss function which controls the number of support vectors, and

Table 8 Performance improvements before and after optimization

Description	$M(x)$	$A(x)$	$G_1(x)$	$G_2(x)$	$E(x)$	$S(x)$
Baseline design	14.150	57.390	14.670	43.870	61,358.750	135.820
Optimum A	12.410	48.570	18.180	40.240	65,348.900	128.400
Improvement (%)	-12.297	-15.368	23.926	-8.274	6.503	-5.463
Optimum B	11.814	54.612	16.820	42.310	62,267.500	127.500
Improvement (%)	-16.509	-4.841	14.656	-3.556	1.481	-6.126
Optimum C	13.911	43.189	21.140	39.090	71,748.521	127.400
Improvement (%)	-1.689	-24.745	44.104	-10.488	16.933	-6.200

Fig. 25 a–d Comparison of the crash pulses before and after optimization



$k(x_i, x_j)$ is the kernel function. The Gaussian kernel function is used herein, which can be expressed as

$$k(x_i, x_j) = \exp\left(-\frac{\|x_i - x_j\|^2}{2\sigma^2}\right) \tag{10}$$

In this study, 980 samples selected from the obtained 1000 samples randomly are used to construct ϵ -SVR models, and the remaining 20 samples are used to validate the prediction accuracy of the constructed surrogate models. The accuracy of the constructed ϵ -SVR models is assessed by using R -square (R^2), relative average absolute error (RAAE), and relative maximum absolute error (RMAE) (Duan et al. 2017a, c; Li et al. 2018). The error results are listed in Table 5. It can be concluded from Table 5 that the constructed ϵ -SVR models are reasonably accurate, and they can be used to substitute the local parametric subsystem front-impact model.

4.6 Results and discussions

The non-dominated sorting genetic algorithm II (NSGA-II) (Deb et al. 2002) is used to solve the MOO problem based on the constructed ϵ -SVR models. For the NSGA-II, the population size, crossover probability, and mutation probability are selected as 20, 0.9, and 0.9, respectively. The crossover

distribution index and mutation distribution index is set as 20, respectively. The optimization is conducted with the 100, 200, 300, and 400 generations, respectively. From which, it is found that the 400 generations converge fairly and stably. Therefore, the Pareto optimal frontier for the MOO problem defined in Eq. (7) is obtained and shown in Fig. 21. We can easily find that the minimization of both the peak acceleration and the weight of the VRB-VCS FLB strongly conflicts with each other.

In order to quantitatively compare the lightweightness and crashworthiness performances for the VRB-VCS FLB and the UT FLB, the best compromise solution (termed as “knee point”), the optimal solutions of mass, and peak acceleration are selected from the Pareto optimal frontier, as shown in Fig. 21. Technique for order preference by similarity to ideal solution (TOPSIS) (Chen and Tzeng 2004) is used to rank the solutions in the Pareto optimal frontier and find the best compromise solution from the Pareto optimal set (i.e., the optimum point A). The optimum point B, located at the top left corner in Fig. 21, is the optimal solution of mass. The optimum point C, located at the bottom right corner in Fig. 21, is the optimal solution of peak acceleration.

The detailed design parameters of the optimal solutions are listed in Table 6. The thickness distributions of the optimized VRB-VCS FLB inner plate (FLB-inner) and the uniform-

thickness FLB inner plate (UT FLB-inner) counterpart are compared in Fig. 22.

Table 6 and Figs. 23 and 24 reveal that the cross-sectional shape and structural characteristics of the optimal FLB are significantly optimized and improved. Moreover, the thickness distributions of the VRB-VCS FLB-inner are all $x_1 < x_2 > x_3$.

The results and relative errors of the selected optimal solutions are listed in Table 7. We can see that the optimal solutions generated from the ϵ -SVRs have sufficient accuracy when compared to the results of FEA. That is to say, the constructed ϵ -SVRs can predict the actual performance accurately.

In this study, the results of FE simulations under the selected optimal solutions are chosen to indicate the performance improvements before and after optimization (see Table 8). The comparison and analysis in Table 8 show the following: (1) the reduction percentages in weight and peak acceleration by optimal solution A relative to the initial state are 12.297% and

15.368%, respectively. At the same time, G_1 increases by 23.926%, and G_2 decreases by 8.274%, with the other performance indices improved by various degrees. (2) The optimal solution B achieves a maximum weight reduction of 16.509% without exceeding the peak acceleration of the initial design. G_1 increases by 14.656%, and G_2 decreases by 3.556%. The energy absorption of the VRB-VCS FLB is improved, and firewall intrusion is reduced. (3) The optimal solution C lowers the peak acceleration by 24.745% without exceeding the initial FLB mass, reducing it from the initial 57.390 g to 43.189 g. G_1 increases by 44.104%, and G_2 decreases by 10.488%. The energy absorption of the VRB-VCS FLB improves by 16.933%, and firewall intrusion decreases by 6.200%.

Figure 25 compares the crash pulses for the local parametric subsystem front-impact model before and after optimization. Figure 25 indicates that the peak accelerations of optimal solutions A, B, and C all decreased in various degrees from those of the initial design state. In addition, the first step acceleration G_1 increased, and the second step acceleration G_2

Fig. 26 Comparison of the deformation patterns of FLB before and after optimization. **a** Left FLB of baseline design. **b** Right FLB of baseline design. **c** Left FLB of optimum A. **d** Right FLB of optimum A. **e** Left FLB of optimum B. **f** Right FLB of optimum B. **g** Left FLB of optimum C. **h** Right FLB of optimum C

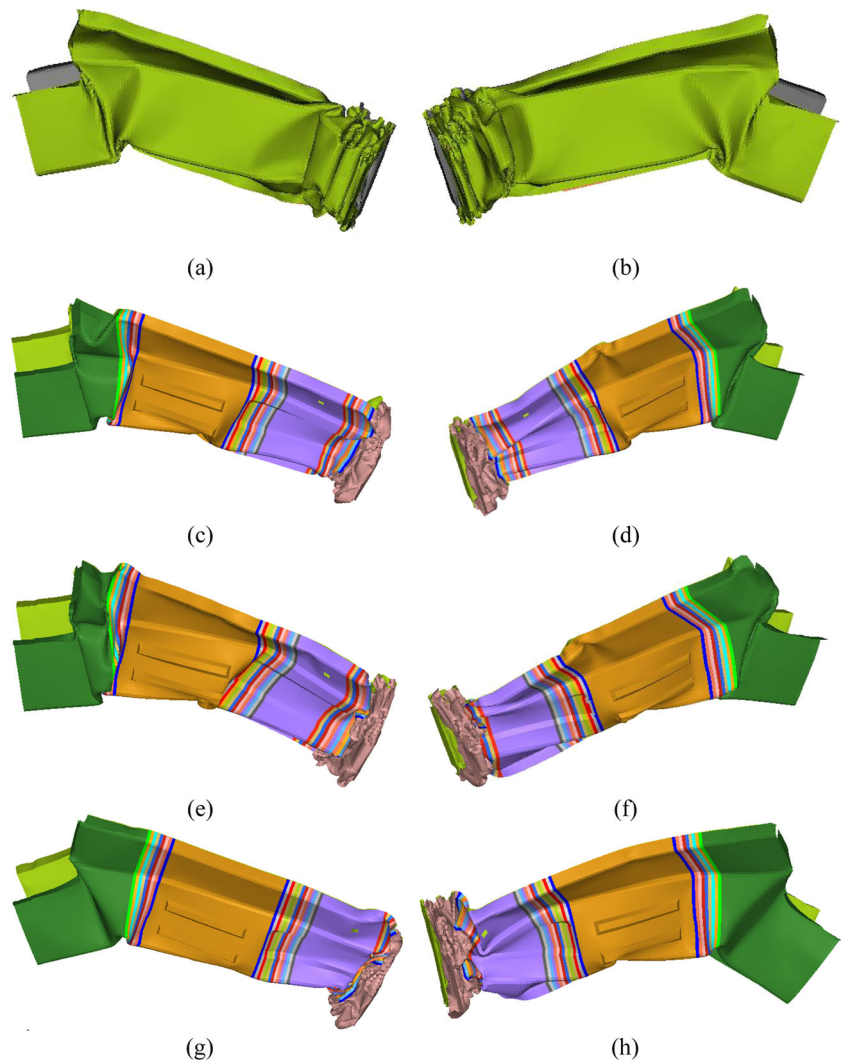
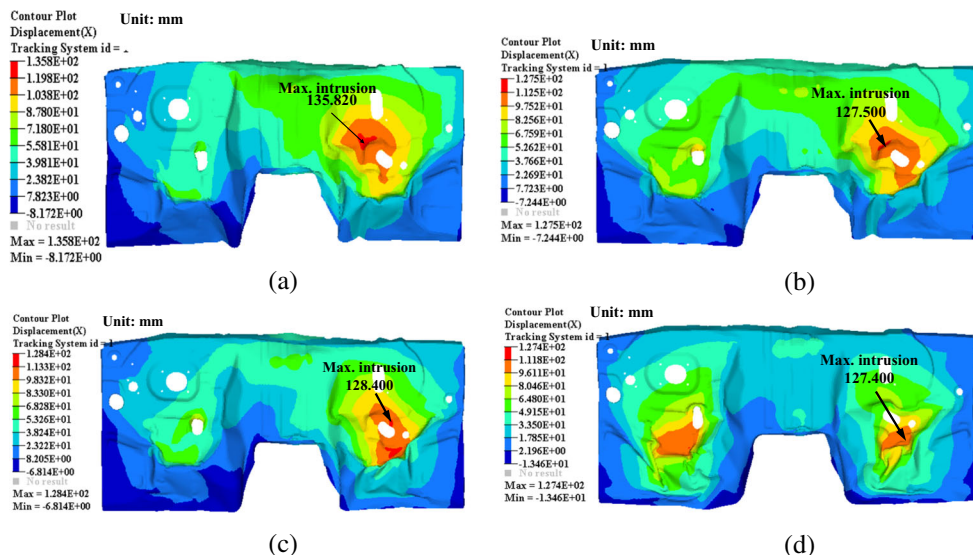


Fig. 27 Comparison of the contour of dash panel intrusions before and after optimization. **a** Baseline design. **b** Optimum A. **c** Optimum B. **d** Optimum C



decreased to different degrees. The amounts of improvement in the crash pulse from largest to smallest are optimal solution A > optimal solution B > optimal solution C.

Figure 26 compares the deformation modes before and after FLB optimization. The key parameters of thickness distribution and cross-sectional shape of the optimized VRB-VCS FLB obtain the optimal FLB deformation modes corresponding to the different design targets. Additionally, the FLB deformation modes of different optimal solutions have three similar characteristics: (a) the progressive crash deformation mode occurs in functional regions A and B to maximize its energy absorption capability, (b) functional region C reduces the crashing force in this segment of the FLB and prevents the peak acceleration from being too high, and (c) functional region D absorbs the residual collision energy.

Figure 27 compares the contour of dash panel intrusions before and after optimization. The maximum intrusion of dash panel decreases a bit when using the optimized VRB-VCS FLBs. From this, it is concluded that the multiobjective crashworthiness optimization of VRB-VCS FLB is more effective in reducing contact injury on occupants caused by dash panel intrusion.

The aforementioned analysis demonstrates that the weight can be largely reduced and/or the crashworthiness performances can be significantly enhanced by appropriate redesigning the wall thicknesses and cross-sectional shape of the VRB-VCS FLB structure, and that the noteworthy lightweightness and crashworthiness performances of the optimized VRB-VCS FLB structures are superior to their UT FLB counterparts. It can be concluded that the VRB-VCS FLB structures can not only keep a better balance between lightweightness and crashworthiness performances but also provide some useful guidance for

designing the other VRB-VCS automotive body structures. The results also provide a reference for application of the VRB-VCS FLB structures in engineering.

5 Conclusions and further work

In this paper, parametric modeling and multiobjective crashworthiness optimization for the VRB-VCS FLB structure under front-impact collision are investigated. Some interesting findings and contributions are summarized as follows:

- (1) A VRB-VCS FLB is proposed, and the construction of a fully parameterized model of the VRB-VCS FLB is also given. As the thickness distribution and cross-sectional shape change continuously, the proposed structure evolves into three distinct forms: the UT FLB, VCS FLB, and VRB FLB. Thus, the VRB-VCS FLB results from the improvement and development in these three structures and combines their advantages to achieve greater generality and more-promising engineering application prospects.
- (2) A local parametric subsystem front-impact model is established to balance accuracy and efficiency. Compared with the full-scale vehicle impact model, the accuracy of the local parametric subsystem front-impact model can be controlled within 3%, and the computation efficiency increased by 46.72%.
- (3) Multiobjective crashworthiness optimization with variable wall thickness and variable cross-sectional shape for design of VRB-VCS FLB structure has been conducted successfully. Firstly, thickness distribution parameters and cross-sectional shape parameters are defined. Secondly, local parametric subsystem front-

impact model is established to improve the updating efficiency of FE model for design points, as well as to reduce their computation time. Finally, a fully automated design of experiment (DOE) platform is established to improve the efficiency of data collection, and epsilon-SVR technique and NSGA-II are utilized to search the Pareto optimal frontier. The numerical results have shown that the reduction percentages in weight and peak acceleration by optimal solution A relative to the initial state are 12.297% and 15.368%, respectively, the optimal solution B achieves a maximum weight reduction of 16.509% without exceeding the peak acceleration of the initial design, and the optimal solution C lowers the peak acceleration by 24.745% without exceeding the initial FLB mass.

- (4) This paper discusses the lightweightness and crashworthiness of a VRB-VCS FLB structure under a 100% front-impact condition. The comprehensive VRB-VCS FLB structure's lightweight and crashworthy design under multiple conditions of 100% frontal, 40% frontal, and 25% frontal small offset collisions are not considered. Because the FLB experiences various collision modes in actual traffic accidents, a multiobjective and multicase-based design optimization for VRB-VCS FLB structures will be important for future studies.

Funding information The authors would like to thank the support of National Natural Science Foundation of China (Grant No. 51805221) and Research Project funded by China Postdoctoral Science Foundation (No. 2018M640460). The authors also wish to thank Jiangsu Planned Projects for Postdoctoral Research Fund (NO. 2018K018C). This work was supported by the high-performance computing platform of Jiangsu University.

Publisher's Note Springer Nature remains neutral with regard to jurisdictional claims in published maps and institutional affiliations.

References

- Alavi Nia A, Parsapour M (2014) Comparative analysis of energy absorption capacity of simple and multi-cell thin-walled tubes with triangular, square, hexagonal and octagonal sections. *Thin Wall Struct* 74:155–165
- Ali M, Ohioma E, Kraft F et al (2015) Theoretical, numerical, and experimental study of dynamic axial crushing of thin walled pentagon and cross-shape tubes. *Thin Wall Struct* 94:253–272
- Alves M (2000) Material constitutive law for large strains and strain rates. *J Eng Mech* 126(2):215–218
- Beik V, Fard M, Jazar R (2016) Crashworthiness of tapered thin-walled S-shaped structures. *Thin Wall Struct* 102:139–147
- Cai K, Wang D (2017a) Optimizing the design of automotive S-rail using grey relational analysis coupled with grey entropy measurement to improve crashworthiness. *Struct Multidiscip O* 56(6):1539–1553
- Cai KF, Wang DF (2017b) Optimizing the design of automotive S-rail using grey relational analysis coupled with grey entropy measurement to improve crashworthiness. *Struct Multidiscip O* 56(6):1539–1553
- Chahardoli S, Nia AA (2017) Investigation of mechanical behavior of energy absorbers in expansion and folding modes under axial quasi-static loading in both experimental and numerical methods. *Thin Wall Struct* 120:319–332
- Chen MF, Tzeng GH (2004) Combining grey relation and TOPSIS concepts for selecting an expatriate host country. *Math Comput Model* 40(13):1473–1490
- Clarke SM, Griebisch JH, Simpson TW (2005) Analysis of support vector regression for approximation of complex engineering analyses. *J Mech Design* 127(6):1077–1087
- Deb K, Pratap A, Agarwal S et al (2002) A fast and elitist multiobjective genetic algorithm: NSGA-II. *Evolutionary Computation, IEEE Transactions* 6:182–197
- Duan LB, Sun GY, Cui JJ et al (2016) Crashworthiness design of vehicle structure with tailor rolled blank. *Struct Multidiscip O* 53(2):321–338
- Duan LB, Xiao NC, Li G et al (2017a) Design optimization of tailor-rolled blank thin-walled structures based on epsilon-support vector regression technique and genetic algorithm. *Eng Optimiz* 49(7):1148–1165
- Duan LB, Xiao NC, Hu ZH et al (2017b) An efficient lightweight design strategy for body-in-white based on implicit parameterization technique. *Struct Multidiscip O* 55(5):1927–1943
- Duan LB, Li GY, Cheng AG et al (2017c) Multi-objective system reliability-based optimization method for design of a fully parametric concept car body. *Eng Optimiz* 49(7):1247–1263
- Duddeck F, Hunkeler S, Lozano P et al (2016) Topology optimization for crashworthiness of thin-walled structures under axial impact using hybrid cellular automata. *Struct Multidiscip O* 54(3):415–428
- Elmarakbi A, Long YX, Macintyre J (2013) Crash analysis and energy absorption characteristics of S-shaped longitudinal members. *Thin Wall Struct* 68:65–74
- Fang JG, Gao YK, Sun GY et al (2015) Dynamic crashing behavior of new extrudable multi-cell tubes with a functionally graded thickness. *Int J Mech Sci* 103:63–73
- Halquist J (2007) LS-DYNA keyword user's manual version 971. Livermore Software Technology Corporation, Livermore
- Hao WQ, Xie JM, Wang FH (2017) Theoretical prediction of the progressive buckling and energy absorption of the sinusoidal corrugated tube subjected to axial crushing. *Comput Struct* 191:12–21
- Hilman J, Paas M, Haenschke A et al (2007) Automatic concept model generation for optimisation and robust design of passenger cars. *Adv Eng Softw* 38(11–12):795–801
- Hou S, Li Q, Long S et al (2008) Multiobjective optimization of multi-cell sections for the crashworthiness design. *Int J Impact Eng* 35(11):1355–1367
- Hunkeler S, Duddeck F, Rayamajhi M et al (2013) Shape optimisation for crashworthiness followed by a robustness analysis with respect to shape variables. *Struct Multidiscip O* 48(2):367–378
- JS P (1994) Optimal Latin-hypercube designs for computer experiments. *J Stat Plan Infer* 39(1):95–111
- Kim JH, Ko DH, Seo PG et al (2014) Limits considering the deformation characteristics of tailor rolled blank during hot stamping. *Trans Mater Process* 23(6):351–356
- Kopp R, Wiedner C, Meyer A (2005) Flexible rolling for load-adapted blanks. *Int Sheet Metal Rev* 4:20–24
- Li GY, Xu FX, Sun GY et al (2015) A comparative study on thin-walled structures with functionally graded thickness (FGT) and tapered tubes withstanding oblique impact loading. *Int J Impact Eng* 77:68–83
- Li Z, Duan LB, Chen T et al (2018) Crashworthiness analysis and multi-objective design optimization of a novel lotus root filled tube (LFT). *Struct Multidiscip O* 57(2):865–875
- Liu XH (2011) Prospects for variable gauge rolling: technology, theory and application. *J Iron Steel Res Int* 18(1):1–7

- Liu S-T, Tong Z-Q, Tang Z-L et al (2014) Design optimization of the S-frame to improve crashworthiness. *Acta Mech Sinica* 30(4):589–599
- Lu RH, Liu XH, Chen S et al (2017) Axial crushing analysis for tailor rolled square tubes with axially graded both wall thickness and material strength. *Thin Wall Struct* 117:10–24
- Meyer A, Wietbrock B, Hirt G (2008) Increasing of the drawing depth using tailor rolled blanks—numerical and experimental analysis. *Int J Mach Tools Manuf* 48(5):522–531
- Mohammadiha O, Ghariblu H (2017) Optimal shape design of functionally graded thickness inversion tubes subjected to oblique loading. *Struct Multidiscip O* 56(3):587–601
- Montoya MC, Costas M, Díaz J et al (2015) A multi-objective reliability-based optimization of the crashworthiness of a metallic-GFRP impact absorber using hybrid approximations. *Struct Multidiscip O* 52(4):827–843
- Nia AA, Hamedani JH (2010) Comparative analysis of energy absorption and deformations of thin walled tubes with various section geometries. *Thin Wall Struct* 48(12):946–954
- Pirmohammad S, Saravani SA (2018) Crashworthiness performance of stiffened foam-filled tapered structures under axial and oblique dynamic loads. *Latin Am J Solids Struct* 15(5):e52
- Qiu N, Gao YK, Fang JG et al (2018) Topological design of multi-cell hexagonal tubes under axial and lateral loading cases using a modified particle swarm algorithm. *Appl Math Model* 53:567–583
- Rais-Rohani M, Solanki K, Eamon C (2006) Reliability-based optimization of lightweight automotive structures for crashworthiness. 11th AIAA/ISSMO multidisciplinary analysis and optimization conference. Portsmouth, Virginia
- Rajabiehfarid R, Darvizeh A, Alitavoli M et al (2016) Experimental and numerical investigation of dynamic plastic behavior of tube with different thickness distribution under axial impact. *Thin Wall Struct* 109:174–184
- Shields MD, Zhang JX (2016) The generalization of Latin hypercube sampling. *Reliab Eng Syst Safe* 148:96–108
- Song XG, Sun GY, Li GY et al (2013) Crashworthiness optimization of foam-filled tapered thin-walled structure using multiple surrogate models. *Struct Multidiscip O* 47(2):221–231
- Sun GY, Xu FX, Li GY et al (2014) Crashing analysis and multiobjective optimization for thin-walled structures with functionally graded thickness. *Int J Impact Eng* 64:62–74
- Tang Z, Liu S, Zhang Z (2012) Energy absorption properties of non-convex multi-corner thin-walled columns. *Thin Wall Struct* 51:112–120
- Tran T (2017) Crushing analysis of multi-cell thin-walled rectangular and square tubes under lateral loading. *Compos Struct* 160:734–747
- Tran T, Hou SJ, Han X et al (2015) Crushing analysis and numerical optimization of angle element structures under axial impact loading. *Compos Struct* 119:422–435
- Usta F, Eren Z, Kurtaran H et al (2018) Crashworthiness optimization of nested and concentric circular tubes using response surface methodology and genetic algorithm. *Latin Am J Solids Struct* 15(5):e42
- Wang D, Cai K (2017) Optimizing the static–dynamic performance of the body-in-white using a modified non-dominated sorting genetic algorithm coupled with grey relational analysis. *Eng Optimiz*:1–19
- Wang W, Qiu XM (2018) Analysis of the carrying capacity for tubes under oblique loading. *J Appl Mech-T Asme* 85(3). <https://doi.org/10.1115/1.4038921>
- Wu SY, Sun GY, Wu X et al (2017) Crashworthiness analysis and optimization of fourier varying section tubes. In *J Non-Linear Mech* 92:41–58
- Xiao N-C, Li Y-F, Yang Y et al (2014) A novel reliability method for structural systems with truncated random variables. *Struct Saf* 50:57–65
- Xiao N-C, Zuo MJ, Zhou C (2018a) A new adaptive sequential sampling method to construct surrogate models for efficient reliability analysis. *Reliab Eng Syst Saf* 1(69):330–338
- Xiao N-C, Zuo MJ, Guo W (2018b) Efficient reliability analysis based on adaptive sequential sampling design and cross-validation. *Appl Math Model* 58:404–420
- Xu FX, Zhang X, Zhang H (2018) A review on functionally graded structures and materials for energy absorption. *Eng Struct* 171:309–325
- Ying L, Dai MH, Zhang SZ et al (2017) Multiobjective crashworthiness optimization of thin-walled structures with functionally graded strength under oblique impact loading. *Thin Wall Struct* 117:165–177
- Zhang X, Zhang H (2013) Theoretical and numerical investigation on the crush resistance of rhombic and kagome honeycombs. *Compos Struct* 96:143–152
- Zhang H, Zhang X (2016) Crashworthiness performance of conical tubes with nonlinear thickness distribution. *Thin Wall Struct* 99:35–44
- Zhang Y, Lu MH, Sun GY et al (2015) On functionally graded composite structures for crashworthiness. *Compos Struct* 132:393–405
- Zimmer H (2010) SFE-CONCEPT reference manual v4, vol 2. SFE-GmbH, Berlin